

# APEX-CHAMP<sup>+</sup> high-*J* CO observations of low-mass young stellar objects

## II. Distribution and origin of warm molecular gas\*

T. A. van Kempen<sup>1,2</sup>, E. F. van Dishoeck<sup>1,3</sup>, R. Güsten<sup>4</sup>, L. E. Kristensen<sup>1</sup>, P. Schilke<sup>4</sup>, M. R. Hogerheijde<sup>1</sup>, W. Boland<sup>1,5</sup>, K. M. Menten<sup>4</sup>, and F. Wyrowski<sup>4</sup>

<sup>1</sup> Leiden Observatory, Leiden University, PO Box 9513, 2300 RA Leiden, The Netherlands

<sup>2</sup> Center for Astrophysics, 60 Garden Street, Cambridge, MA 02138, USA  
e-mail: tvankempen@cfa.harvard.edu

<sup>3</sup> Max-Planck Institut für Extraterrestrische Physik (MPE), Giessenbachstr. 1, 85748 Garching, Germany

<sup>4</sup> Max Planck Institut für Radioastronomie, Auf dem Hügel 69, 53121 Bonn, Germany

<sup>5</sup> Nederlandse Onderzoeksschool Voor Astronomie (NOVA), PO Box 9513, 2300 RA Leiden, The Netherlands

<sup>6</sup> SRON Netherlands Institute for Space Research, PO Box 800, 9700 AV Groningen, The Netherlands

Received 15 May 2009 / Accepted 18 August 2009

### ABSTRACT

**Context.** The origin and heating mechanisms of warm ( $50 < T < 200$  K) molecular gas in low-mass young stellar objects (YSOs) are strongly debated. Both passive heating of the inner collapsing envelope by the protostellar luminosity as well as active heating by shocks and by UV associated with the outflows or accretion have been proposed. Most data so far have focussed on the colder gas component.

**Aims.** We aim to characterize the warm gas within protostellar objects, and disentangle contributions from the (inner) envelope, bipolar outflows and the quiescent cloud.

**Methods.** High-*J* CO maps ( $^{12}\text{CO}$   $J = 6-5$  and  $7-6$ ) of the immediate surroundings (up to 10 000 AU) of eight low-mass YSOs are obtained with the CHAMP<sup>+</sup> 650/850 GHz array receiver mounted on the APEX telescope. In addition, isotopologue observations of the  $^{13}\text{CO}$   $J = 6-5$  transition and [C I]  $^3\text{P}_2 - ^3\text{P}_1$  line were taken.

**Results.** Strong quiescent narrow-line  $^{12}\text{CO}$   $6-5$  and  $7-6$  emission is seen toward all protostars. In the case of HH 46 and Ced 110 IRS 4, the on-source emission originates in material heated by UV photons scattered in the outflow cavity and not just by passive heating in the inner envelope. Warm quiescent gas is also present along the outflows, heated by UV photons from shocks. This is clearly evident in BHR 71 for which quiescent emission becomes stronger at more distant outflow positions. Shock-heated warm gas is only detected for Class 0 flows and the more massive Class I sources such as HH 46. Outflow temperatures, estimated from the CO  $6-5$  and  $3-2$  line wings, are  $\sim 100$  K, close to model predictions, with the exception of the L 1551 IRS 5 and IRAS 12496-7650, for which temperatures  $< 50$  K are found.

**Conclusions.** APEX-CHAMP<sup>+</sup> is uniquely suited to directly probe the protostar's feedback on its accreting envelope gas in terms of heating, photodissociation, and outflow dispersal by mapping  $\sim 1' \times 1'$  regions in high-*J* CO and [C I] lines. Photon-heating of the surrounding gas may prevent further collapse and limit stellar growth.

**Key words.** astrochemistry – stars: formation – ISM: jets and outflows – submillimeter – stars: circumstellar matter – stars: pre-main sequence

## 1. Introduction

Low-mass ( $M < 3 M_\odot$ ) Stage 0 and Stage 1 protostars (Robitaille et al. 2006) have two distinct components. First, they are surrounded by a protostellar envelope, consisting of a reservoir of gas and dust, which can feed the star and disk. The envelope can be divided into cold ( $T \sim 10-20$  K) outer regions and a warm ( $T > 50$  K) inner region (Adams et al. 1987; Shirley et al. 2000; Schöier et al. 2002; Shirley et al. 2002; Jørgensen et al. 2002; Whitney et al. 2003a; Robitaille et al. 2006). Second, most, if not all, embedded protostars have molecular outflows

(Bachiller 1996; Bachiller & Tafalla 1999; Arce & Sargent 2005; Lee & Ho 2005; Hirano et al. 2006). These outflows have been observed to have a wide variety in intensity, collimation and affected area, ranging from the strong and large (ten thousands of AU) outflows seen in L 1448, L 1551 IRS 5 and HH 46 (e.g., Bachiller et al. 1994; Heathcote et al. 1996; van Kempen et al. 2009, from here on referred to as Paper I) to the weak, much more compact, outflows as found for TMR 1 and TMC-1 (Cabrit & Bertout 1992; Hogerheijde et al. 1998). Such molecular outflows are observed to widen with time and influence the evolution of the envelope (e.g., Arce & Sargent 2005).

Envelope models can be constructed using either a 1-D or 2-D self-consistent dust radiative transfer calculation, constrained by observations of the cold dust (e.g. Shirley et al. 2002; Jørgensen et al. 2002) and/or the spectral energy distribution

\* Fits files of data used in constructing maps are only available in electronic form at the CDS via anonymous ftp to cdsarc.u-strasbg.fr (130.79.128.5) or via <http://cdsweb.u-strasbg.fr/cgi-bin/qcat?J/A+A/507/1425>

(SED) (e.g. Whitney et al. 2003b,a; Robitaille et al. 2006; Crapsi et al. 2008). Combining heterodyne observations with radiative transfer calculations, one can in turn analyze line emission of a large range of molecules and determine their origin and excitation conditions, both in the inner and outer regions of protostellar envelopes as well as in circumstellar disks and foreground components (e.g. Boogert et al. 2002; Jørgensen 2004; Maret et al. 2004; Brinch et al. 2007; Lee et al. 2007). Envelope models predict that the inner regions are warm ( $T > 100$  K), dense ( $n(\text{H}_2) > 10^6 \text{ cm}^{-3}$ ) and relatively small ( $R < 500$  AU). Most molecular lines observable at (sub)mm wavelengths trace the colder gas, but a few lines, such as the high- $J$  CO lines, directly probe the warm gas. The atmospheric windows at 650 and 850 GHz are the highest frequency windows in which observations of CO (up to energy levels of  $\sim 150$  K) can be routinely carried out. Unfortunately, few studies have successfully observed CO transitions or its isotopologues in these atmospheric windows due to the excellent weather conditions necessary. In addition, such studies are often limited to single spectra of only a handful of YSOs (e.g. Schuster et al. 1993, 1995; Hogerheijde et al. 1998; Ceccarelli et al. 2002; Stark et al. 2004; Parise et al. 2006; van Kempen et al. 2006). The lack of spatial information on the warm gas distribution has prevented an in-depth analysis. Comparison between ground-based high- $J$  CO observations and far-IR CO transitions (CO 15–14 and higher) do not always agree on the origin of the high- $J$  CO lines (van Kempen et al. 2006).

Complex molecules such as H<sub>2</sub>CO and CH<sub>3</sub>OH, emit in high excitation lines at longer wavelengths, and have been observed to have surprisingly high abundances in low-mass protostars (e.g. van Dishoeck et al. 1995; Blake et al. 1995; Ceccarelli et al. 2000; Schöier et al. 2002; Maret et al. 2004; Jørgensen 2004; Bottinelli et al. 2004, 2007). Unfortunately, the abundances of these molecules are influenced by the gas-phase and grain surface chemistry, complicating their use as tracers of the physical structure (e.g., Bisschop et al. 2007). It has been proposed that the emission of such molecules originates inside a hot core region, a chemically active area close to the star, coinciding with the passively heated warm inner region of the protostellar envelope where ices have evaporated (Ceccarelli et al. 2000; Bottinelli et al. 2004, 2007). However, to fully understand the origin of these complex organics, knowledge of the structure of the warm gas is an essential ingredient.

Warm gas near protostars can have different origins than passive heating alone. Outflow shocks passing through the envelope can be a source of heat. Quiescent gas, heated by X-rays or UV, is present in the inner envelope. For example, Stäuber et al. (2004) show that significant amounts of far ultra-violet (FUV) or X-ray photons are necessary to reproduce the line intensities and the derived abundances of molecules, such as CO<sup>+</sup>, CN, CH<sup>+</sup> and NO in both high and low-mass protostars. Spaans et al. (1995) investigated photon heating of outflow cavity walls to reproduce the observed line intensities and widths of <sup>12</sup>CO 6–5 and <sup>13</sup>CO 6–5 emission in Class I sources (Hogerheijde et al. 1998). In Paper I, an extension of this model is proposed in which a Photon Dominated Region (PDR) at the outflow/envelope cavity walls is present in the HH 46 outflow to explain the relatively strong and quiescent high- $J$  CO emission. The emission of [C I] can constrain the color and extent of the more energetic photons. Apart from the accretion disk, UV photons are also produced by the jet shocks in the outflow cavity and the outflow bow shock. All these models provide different predictions for the spatial extent of the warm gas ( $\sim 1'$  for the outflow to  $< 1''$  for a passively

heated envelope), as well as the different integrated intensities and line profiles of the high- $J$  CO transitions.

The most direct tracers of the warm ( $50 < T < 200$  K) gas are thus the high- $J$  CO lines. So far, studies to directly detect the warm gas components through these lines have rarely been able to disentangle the envelope and outflow contributions. Far infrared (IR) transitions of even higher- $J$  CO, the far-IR CO lines, have been observed using the ISO-LWS instrument to trace the inner regions (e.g., Ceccarelli et al. 1998; Giannini et al. 1999; Nisini et al. 1999; Giannini et al. 2001; Nisini et al. 2002), but could not unambiguously constrain the origin of the warm gas emission, due to the limited spatial and spectral resolution.

The Chajnantor plateau in northern Chile, where the recently commissioned Atacama Pathfinder EXperiment (APEX)<sup>1</sup> is located, currently is the only site able to perform routine observations within the high frequency atmospheric windows at high ( $\leq 10''$ ) spatial resolutions. The CHAMP<sup>+</sup> instrument, developed by the MPIfR and SRON Groningen, is the only instrument in the world able to simultaneously observe molecular line emission in the 650 and 850 GHz atmospheric windows on sub-arcminute spatial scales and is thus ideally suited to probe the warm gas directly through observations of the 6–5, 7–6 and 8–7 transitions of CO and its isotopologues with 7–9'' angular resolution (Kasemann et al. 2006; Güsten et al. 2008). CHAMP<sup>+</sup> has 14 pixels (7 in each frequency window) and is thus capable of fast mapping of the immediate surroundings of embedded YSOs. The *Herschel Space Observatory* will allow observations of far-IR CO lines at spectral and spatial resolution similar to APEX ( $\sim 10''$ ). Note also that the beam of Herschel is comparable or smaller than the field of view of CHAMP<sup>+</sup> at its longer wavelengths ( $\sim 500 \mu\text{m}$ ). Thus the CHAMP<sup>+</sup> data obtained here provide information of the distribution of warm gas within the Herschel beams.

In Paper I, we presented the results for one source, HH 46 IRS. In this paper, we present observations of CO and its isotopologues using CHAMP<sup>+</sup> for seven additional embedded YSOs and compare them with the HH 46 case. Section 2 presents the sample and observations. The resulting spectral maps are shown in Sect. 3. Section 4 discusses the envelope and outflow structure, while the heating within protostellar envelopes and molecular outflows is analyzed in Sect. 5. Section 6 investigates the relation between the emission of more complex molecules and the emission of high- $J$  CO. Final conclusions are given in Sect. 7.

## 2. Sample and observations

### 2.1. Observations

The sample was observed using the CHAMP<sup>+</sup> array (Kasemann et al. 2006; Güsten et al. 2008) on APEX (Kasemann et al. 2006). CHAMP<sup>+</sup> observes simultaneously in the 650 GHz (450  $\mu\text{m}$ , CHAMP<sup>+</sup>-I) and 850 GHz (350  $\mu\text{m}$ , CHAMP<sup>+</sup>-II) atmospheric windows. The array has 7 pixels for each frequency, arranged in a hexagon of 6 pixels around 1 central pixel, for a total of 14 pixels. During the observations, the backend consisted of 2 Fast Fourier Transform Spectrometer (FFTS) units serving the central pixel, and 12 MPI-Auto-Correlator Spectrometer (MACS) units serving the other pixels. The FFTS units are capable of observing up to a resolution of  $0.04 \text{ km s}^{-1}$  (0.12 MHz) and the

<sup>1</sup> This publication is based on data acquired with the Atacama Pathfinder Experiment (APEX). APEX is a collaboration between the Max-Planck-Institut für Radioastronomie, the European Southern Observatory, and the Onsala Space Observatory.

MACS units to a spectral resolution of  $0.37 \text{ km s}^{-1}$  (1 MHz), both at a frequency of 806 GHz. The observations were done during three observing runs in June 2007, October–November 2007 and July 2008 in three different line settings; see Table 1. Note that in July 2008, all pixels were attached to FFTS units and no MACS backends were used. For mapping purposes, the array was moved in a small hexagonal pattern to provide a fully Nyquist sampled map or in an on-the-fly (OTF) mode. The “hexa” pattern covers a region of about  $30'' \times 30''$ . For some sources, a slightly larger area was mapped in a small OTF ( $40'' \times 40''$ ) map in  $^{12}\text{CO}$  6–5/7–6. Both kinds of maps were regredded to a regular grid with standard rebinning algorithms included in the CLASS package<sup>2</sup>. A binning method that uses equal weight binning was adopted to produce contour maps. A pixelsize of 1/3rd of the beamsize was adopted to create accurate contour maps. CLASS was also used as the main reduction package for individual lines. At the edge of the maps, noise levels are often higher due to the shape of the CHAMP<sup>+</sup> array. NGC 1333 IRAS 2, TMR 1 and RCRA IRS 7 were observed using the hexa mode and have smaller covered areas. Due to the different beams at 690 and 800 GHz, small differences exist between the areas covered in CO 6–5 and 7–6. For the  $\text{C}^{18}\text{O}$  6–5/ $^{13}\text{CO}$  8–7 (setting C; only done for HH 46), a stare mode was used to increase the S/N within the central pixel. A position switch of  $900''$  was used for all settings, except for the stare setting C, which used a beam-switching of  $90''$ .

Beam efficiencies, derived using observations on planets during each run, are 0.56 for CHAMP<sup>+</sup>-I and 0.43 for CHAMP<sup>+</sup>-II. These efficiencies were found to vary by less than 10% over a single observing run and between runs. Between pixels the variation is similar, all within 10%. Depending on observing mode, a given sky position is covered by many (all) pixels, so the average (relative) calibration error will be a few per cent. Typical single side-band system temperatures are 700 K for CHAMP<sup>+</sup>-I and 2100 K for CHAMP<sup>+</sup>-II. The 12-m APEX dish produces a beam of  $9''$  at 650 GHz and  $7''$  at 850 GHz. Pointing was checked on various planets and sources and was found to be within  $3''$ . Calibration of the sources was done using similar observations, as well as hot and cold loads. The typical sideband rejection at both frequencies was measured to be less than 10dB. At APEX 10 dB is used as the input to the calibrator (both continuum and line). From all these effects, the total calibration error is estimated to be  $\sim 30\%$ , including the atmospheric model. Note that all technical aspects of CHAMP<sup>+</sup> will be discussed more extensively in Güsten et al. (to be submitted to A&A, see also Güsten et al. 2008).

The difference in CO 7–6 emission of 60% for IRAS 12496–7650 in van Kempen et al. (2006) and this paper can be accounted for by the respective calibration and pointing errors of FLASH and CHAMP<sup>+</sup>. A factor of 2 difference is found with the observations of TMR 1 in Hogerheijde et al. (1998). Since a similar factor of 2 is seen between the observations of T Tau in Schuster et al. (1995) and Hogerheijde et al. (1998), it is most likely that the side-band gain ratios for the observations taken by Hogerheijde et al. (1998) were incorrectly calibrated.

## 2.2. Sample

The sample consists of eight well-known and well-studied embedded protostars, with a slight bias toward the southern sky.

A variety of protostars in mass, luminosity, evolutionary stage and parental cloud is included. All sources have been studied in previous surveys of embedded YSOs in the sub-mm (e.g., Jørgensen et al. 2002, 2004; Groppi et al. 2007). More information on southern sources can be found in van Kempen et al. (2006) (IRAS 12496–7650), van Kempen et al. 2009 submitted (IRAS 12496–7650, RCRA IRS 7 and Ced 110 IRS 4) and Paper I (HH 46). Table 2 gives the parameters of each source and its properties. References to previous continuum studies (Col. 7) include infrared (IR) and (sub)millimeter dust continuum photometry, and studies of CO emission (Col. 8) include both sub-millimeter and far-IR lines. Note that the binary source of N1333 IRAS 2A, N1333 IRAS 2B is not covered by our map.

## 2.3. Spectral energy distribution

For all sources, SED information was acquired from the literature, ranging from near-IR to the (sub-)mm wavelengths. Spitzer-IRAC (3.6, 4.5, 5.6, 8.0  $\mu\text{m}$ ), Spitzer-MIPS (24, 70 and 160  $\mu\text{m}$ ), submillimeter photometry from JCMT/SCUBA (Di Francesco et al. 2008), SEST/SIMBA and IRAM-30m/MAMBO are all included, if available. For sources with no reliable Spitzer fluxes, IRAS fluxes at 12, 25, 60 and 100  $\mu\text{m}$  were used. In addition to the obtained fluxes, the bolometric luminosity and temperature,  $L_{\text{bol}}$  and  $T_{\text{bol}}$  were calculated using the mid-point method (Dunham et al. 2008). The results can be found in Table 2. Note that due to a lack of mid- and far-IR fluxes with sufficient spatial resolution, the derived values for IRAS 12496–7650 and Ced 110 IRS 4 are highly uncertain, with expected errors of 50%, while no  $T_{\text{bol}}$  and  $L_{\text{bol}}$  could be determined for RCRA IRS 7 due to confusion. For other sources, errors are on the order of 10–20%.

## 3. Results

### 3.1. Maps

Figures 1 to 8 show the integrated intensity and the red- and blue-shifted outflow emission mapped in the CO 6–5 line, as well as the spectra at the central position of all observed emission lines. Both the integrated intensity and outflow maps were spatially rebinned to a resolution of  $10''$ . Figures 9 to 12 show the CO 6–5 and 7–6 spectra taken in the inner  $40'' \times 40''$  of all the sources, also binned to square  $10'' \times 10''$  bins.

Table 3 presents the intensities of both CO lines. Here, the total integrated emission, the peak main beam temperature, the emission in the red and blue outflow wings shown in the outflow maps and the noise levels are given for the central position, as well as at positions with clear detections of outflow wings away from the center. The limits for the red and blue outflow were chosen to be  $-10$  to  $-1.5 \text{ km s}^{-1}$  with respect to the source velocity for the blueshifted emission and  $+1.5$  to  $+10 \text{ km s}^{-1}$  with respect to the source velocity for the redshifted emission for most sources. These limits were chosen after examination of the profiles of the spectra and subtracting Gaussians that were fitted to the central  $3 \text{ km s}^{-1}$  of the profile. For all sources, except RCRA IRS 7, the difference in the blue- and red-shifted emission between the two methods was less than 5%. The outflowing gas of RCRA IRS 7 was derived by limiting the red- and blue-shifted emission to  $-20$  to  $-8$  and  $+8$  to  $+20 \text{ km s}^{-1}$  from line center. This corresponds to a  $FWHM \approx 8 \text{ km s}^{-1}$  for the quiescent material. Broad line widths of  $3 \text{ km s}^{-1}$  are also seen for the rarer isotopologues  $\text{C}^{18}\text{O}$  and  $\text{C}^{17}\text{O}$ , much wider than typically observed for these species in low-mass YSOs (Schöier et al. 2006). Noise levels (see Table 3) differ greatly between sources and even within single maps.

<sup>2</sup> CLASS is part of the GILDAS reduction package.

See <http://www.iram.fr/IRAMFR/GILDAS> for more information.

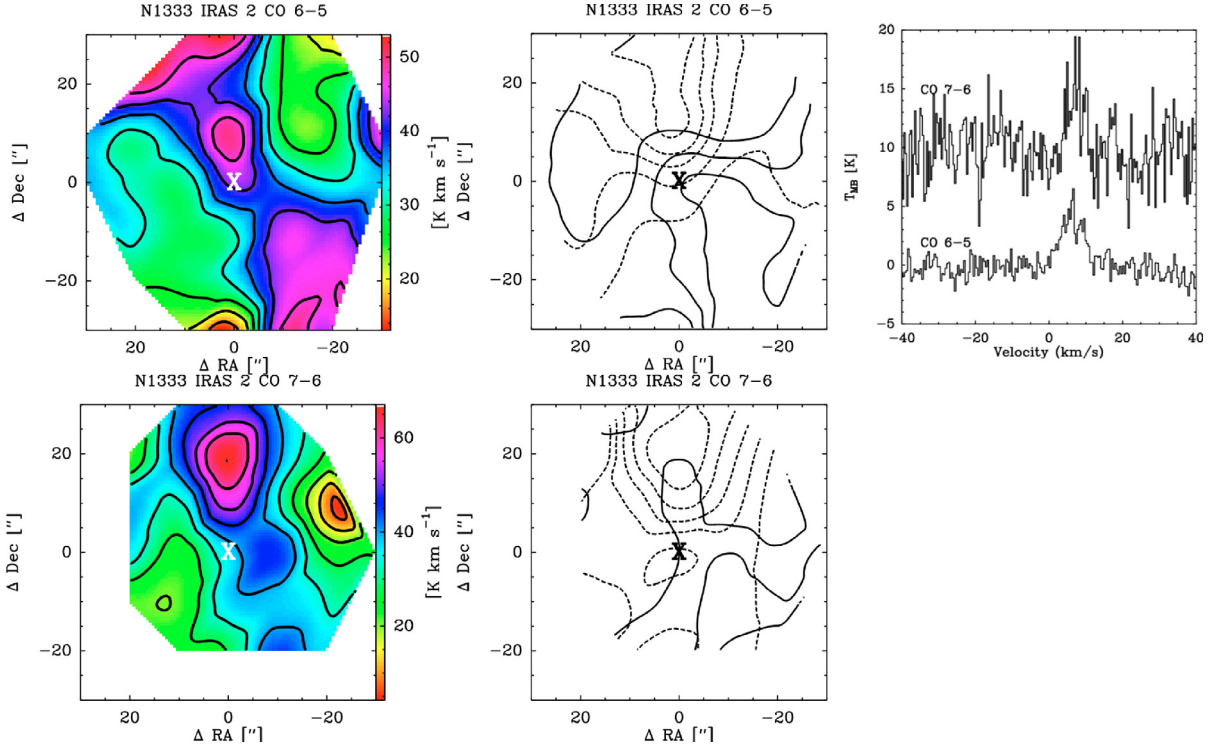


**Fig. 1.** Maps of CO 6–5 (top row) and CO 7–6 (bottom row) of NGC 1333 IRAS 2. The left-most image shows the total integrated intensity over the line. The middle figures show the outflow contributions from the red (dashed lines) and blue (solid lines) outflow. Contours are in increasing levels of  $4 \text{ K km s}^{-1}$  for both transitions. The outflow contributions are calculated by only including emission greater or smaller than  $\pm 1.5 \text{ km s}^{-1}$  from the central velocity. The right-most image at the top row shows the  $^{12}\text{CO}$  spectra at the central position.

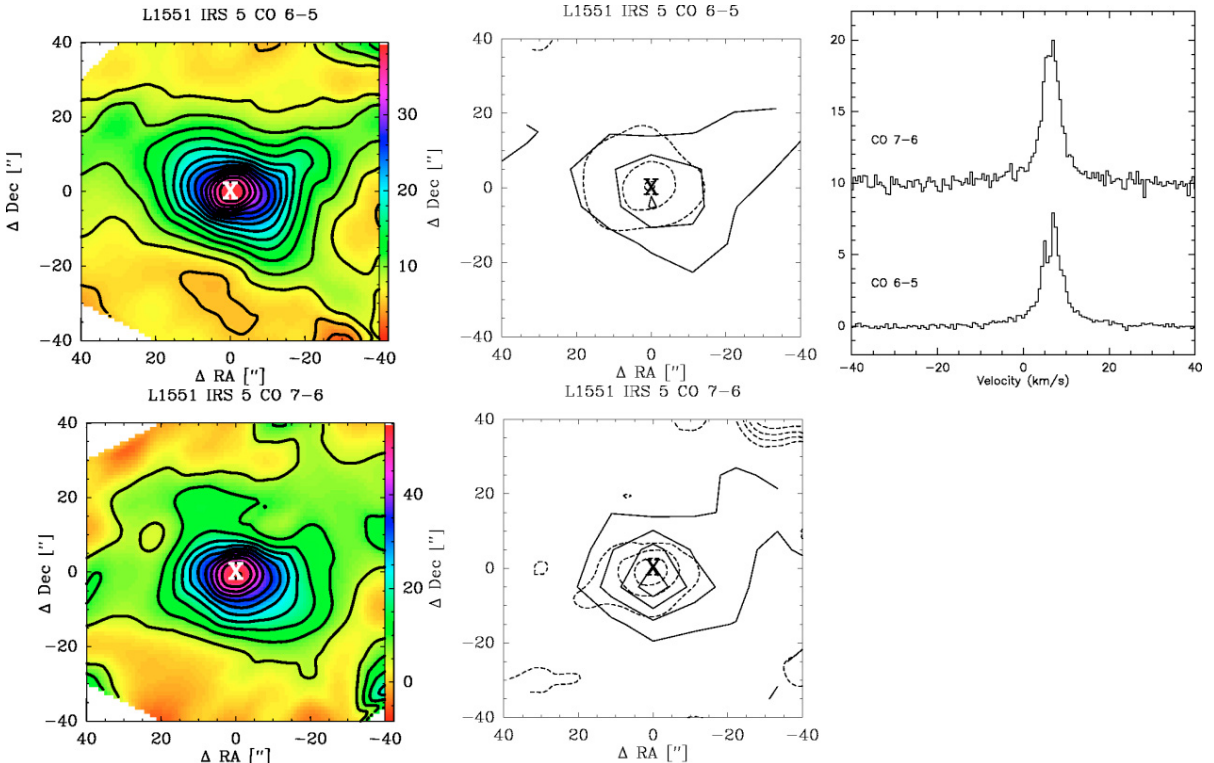


**Fig. 2.** Maps of CO 6–5 (top row) and CO 7–6 (bottom row) of L 1551 IRS 5. The left-most image shows the total integrated intensity over the line. The middle figures show the outflow contributions from the red (dashed lines) and blue (solid lines) outflow. Contours are in increasing levels of  $0.5 \text{ K km s}^{-1}$  for both transitions. The outflow contributions are calculated by only including emission greater or smaller than  $\pm 1.5 \text{ km s}^{-1}$  from the central velocity. The right-most image at the top row shows the  $^{12}\text{CO}$  spectra at the central position.

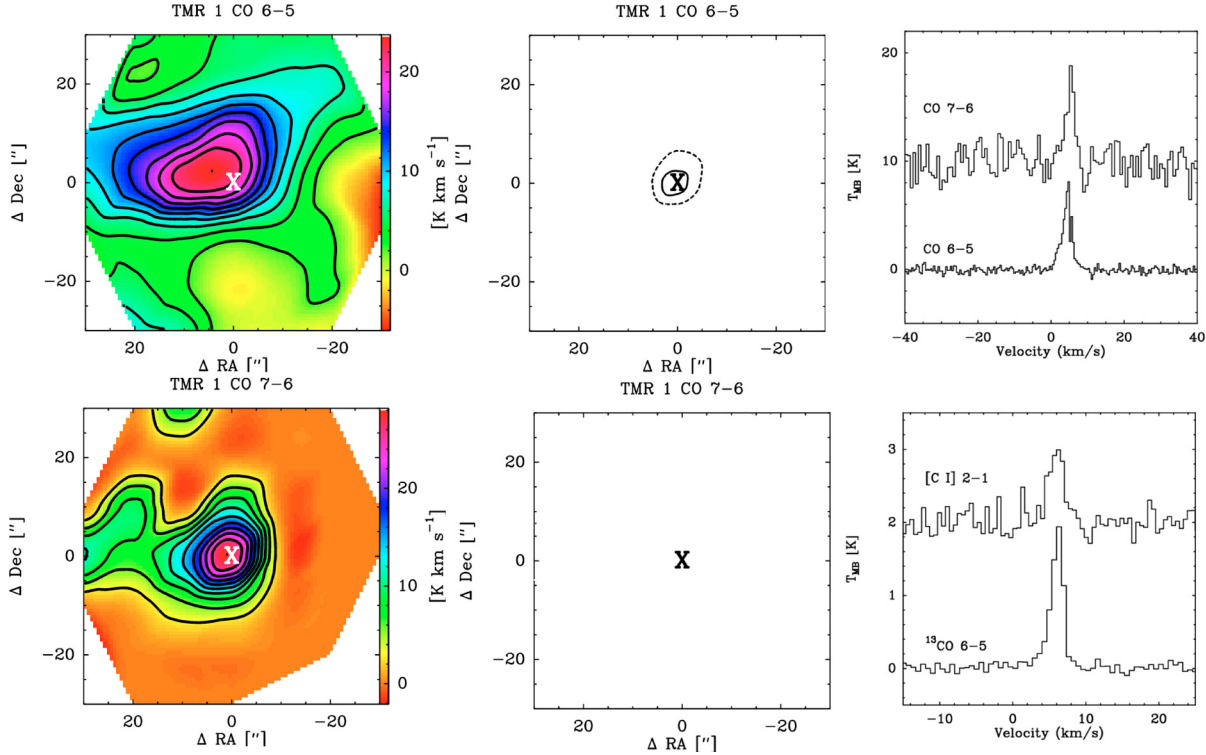


**Fig. 3.** Maps of CO 6–5 (top row) and CO 7–6 (bottom row) of TMR 1. The left-most image shows the total integrated intensity over the line. The middle figures show the outflow contributions from the red (dashed lines) and blue (solid lines) outflow. Contours are in increasing levels of  $1 \text{ K km s}^{-1}$  for both transitions. The outflow contributions are calculated by only including emission greater or smaller than  $\pm 1.5 \text{ km s}^{-1}$  from the central velocity. The right-most image at the top row shows the  $^{12}\text{CO}$  spectra at the central position, while the right-most image at the bottom row shows the spectra of the observed isotopologues and [C I] 2–1 at the central position.

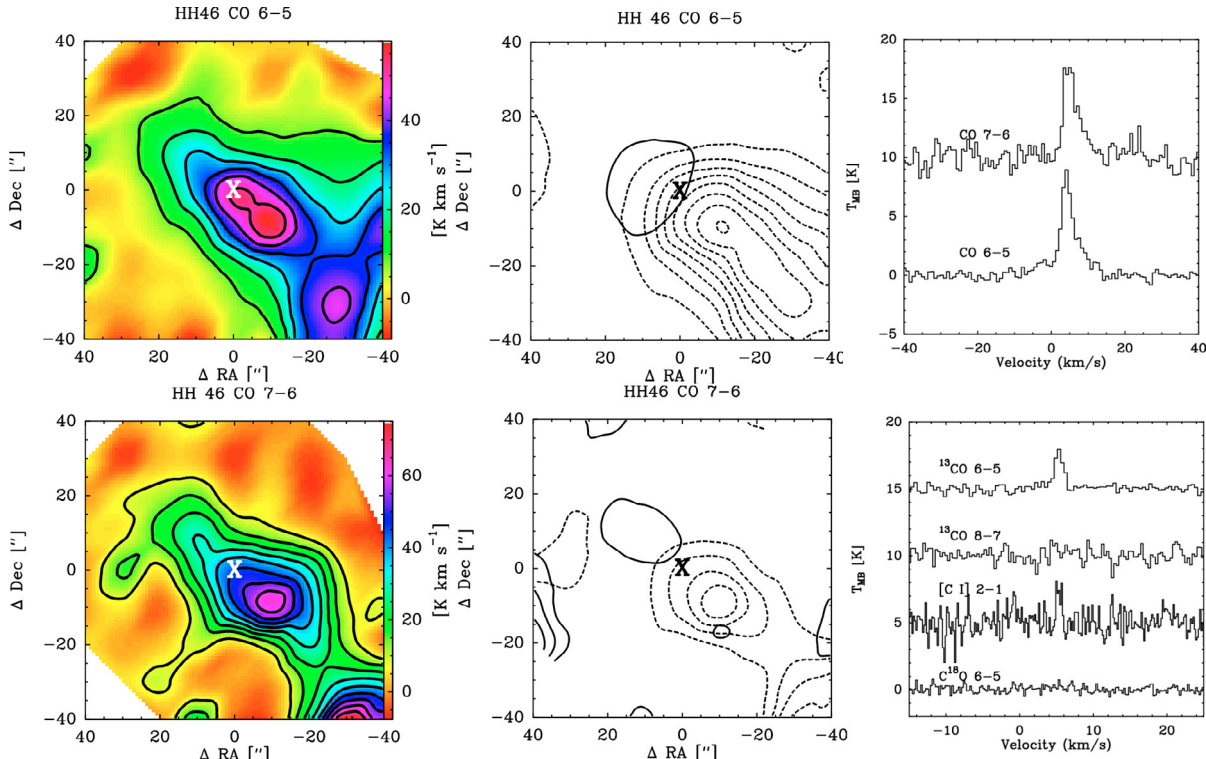


**Fig. 4.** CO 6–5 (left) CO 7–6 (middle) maps and spectra of the central position of HH 46. The left-most image shows the total integrated intensity over the line. The middle figures show the outflow contributions from the red (dashed lines) and blue (solid lines) outflow. Contours are in increasing levels of  $2 \text{ K km s}^{-1}$  for CO 6–5 and  $3 \text{ K km s}^{-1}$  for CO 7–6. The outflow contributions are calculated by only including emission greater or smaller than  $\pm 1.5 \text{ km s}^{-1}$  from the central velocity. The right-most image at the top row shows the  $^{12}\text{CO}$  spectra at the central position, while the right-most image at the bottom row shows the spectra of the observed isotopologues and [C I] 2–1 at the central position (see also Paper I).

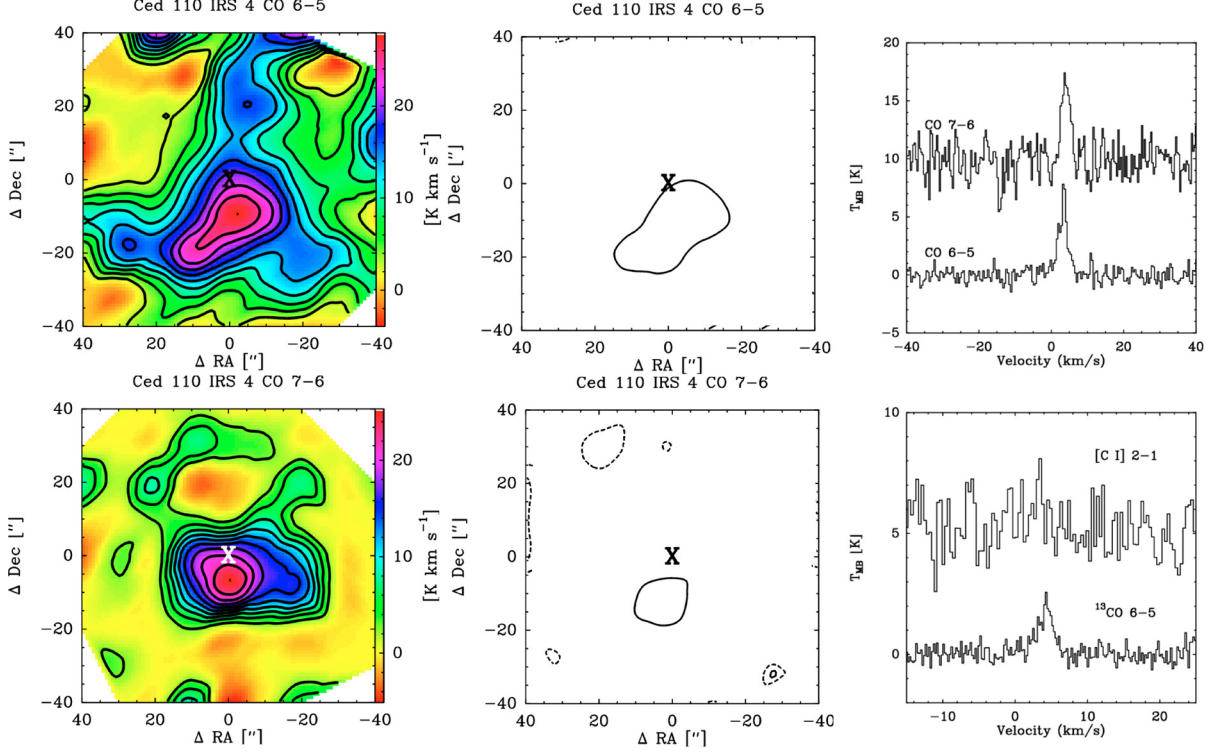


**Fig. 5.** Maps of CO 6–5 (top row) and CO 7–6 (bottom row) of Ced 110 IRS 4. The left-most image shows the total integrated intensity over the line. The middle figures show the outflow contributions from the red (dashed lines) and blue (solid lines) outflow. Contours are in increasing levels of  $3 \text{ K km s}^{-1}$  for both transitions. The outflow contributions are calculated by only including emission greater or smaller than  $\pm 1.5 \text{ km s}^{-1}$  from the central velocity. The right-most image at the top row shows the  $^{12}\text{CO}$  spectra at the central position, while the right-most image at the bottom row shows the spectra of the observed isotopologues and [C I] 2–1 at the central position.

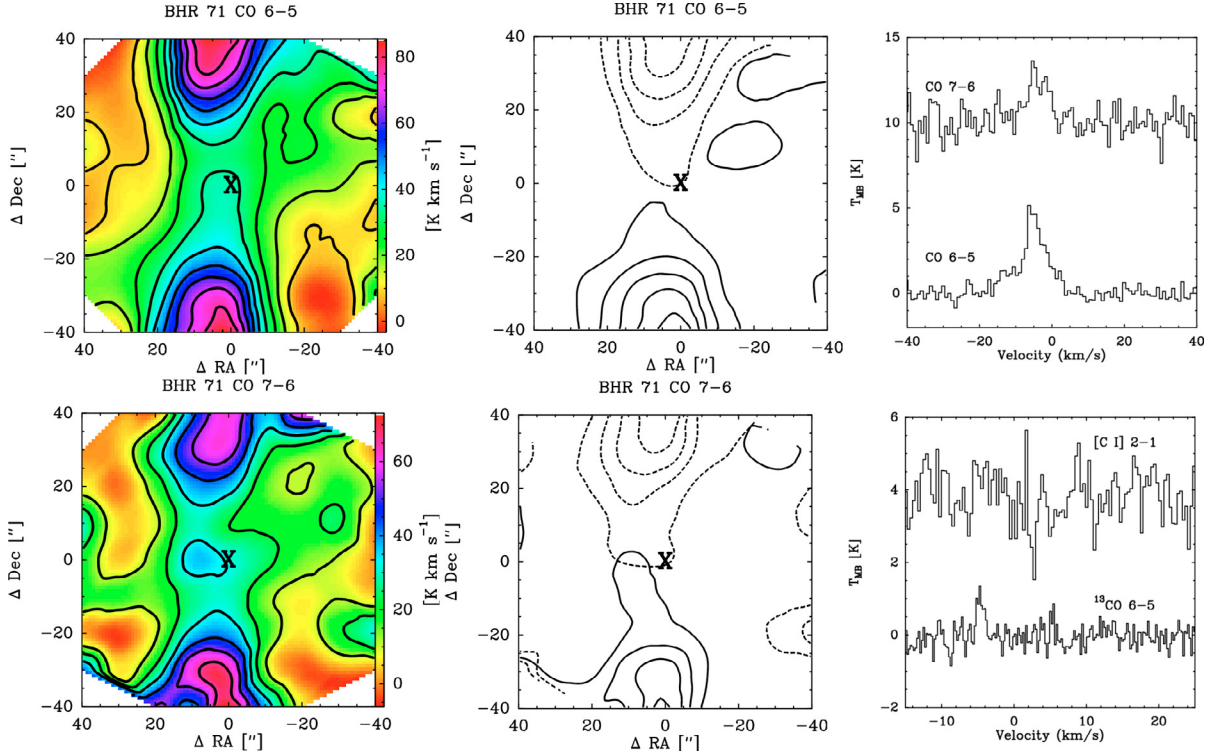


**Fig. 6.** Maps of CO 6–5 (top row) and CO 7–6 (bottom row) of BHR 71. The left-most image shows the total integrated intensity over the line. The middle figures show the outflow contributions from the red (dashed lines) and blue (solid lines) outflow. Contours are in increasing levels of  $10 \text{ K km s}^{-1}$  for CO 6–5 and  $5 \text{ K km s}^{-1}$  for CO 7–6. The outflow contributions are calculated by only including emission greater or smaller than  $\pm 1.5 \text{ km s}^{-1}$  from the central velocity. The right-most image at the top row shows the  $^{12}\text{CO}$  spectra at the central position, while the right-most image at the bottom row shows the spectra of the observed isotopologues and [C I] 2–1 at the central position.

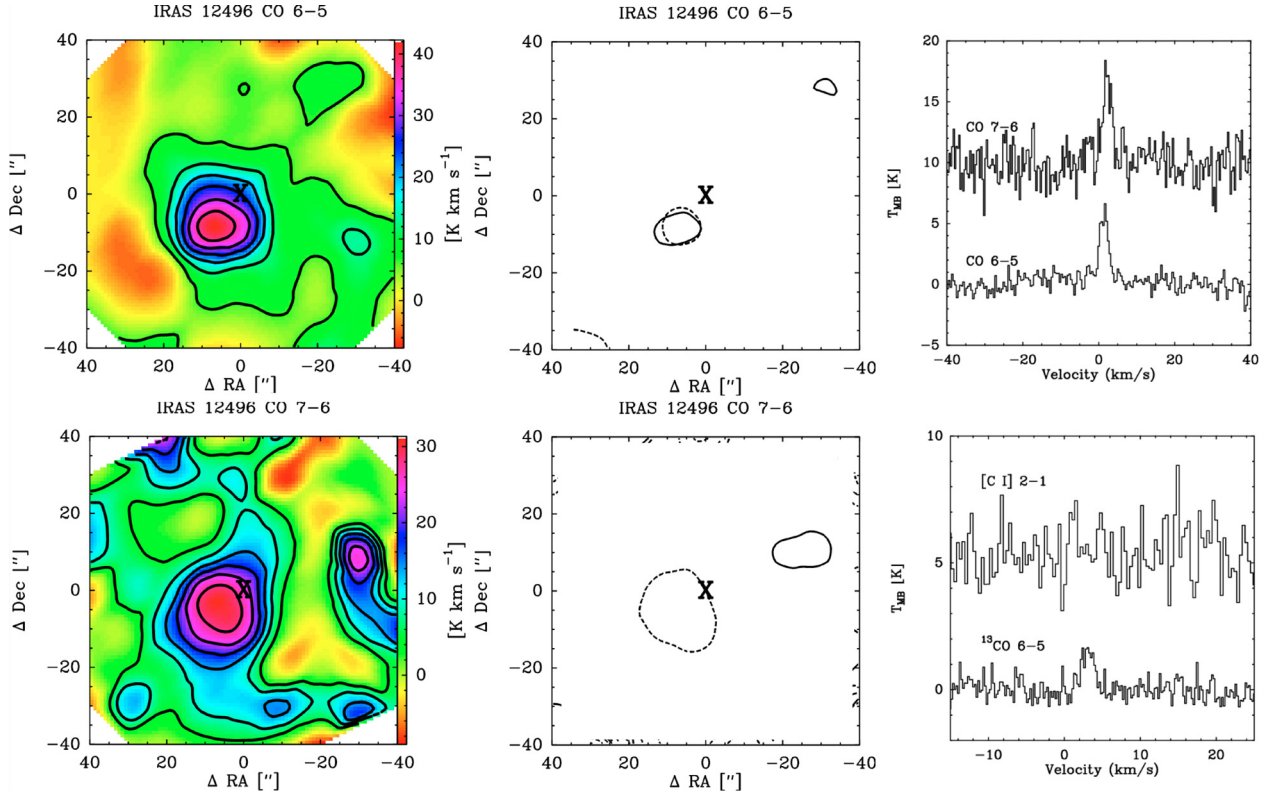


**Fig. 7.** Maps of CO 6–5 (top row) and CO 7–6 (bottom row) of IRAS 12496-7650. The left-most image shows the total integrated intensity over the line. The middle figures show the outflow contributions from the red (dashed lines) and blue (solid lines) outflow. Contours are in increasing levels of  $3 \text{ K km s}^{-1}$  for both transitions. The outflow contributions are calculated by only including emission greater or smaller than  $\pm 1.5 \text{ km s}^{-1}$  from the central velocity. The right-most image at the top row shows the  $^{12}\text{CO}$  spectra at the central position, while the right-most image at the bottom row shows the spectra of the observed isotopologues and [C I] 2–1 at the central position.

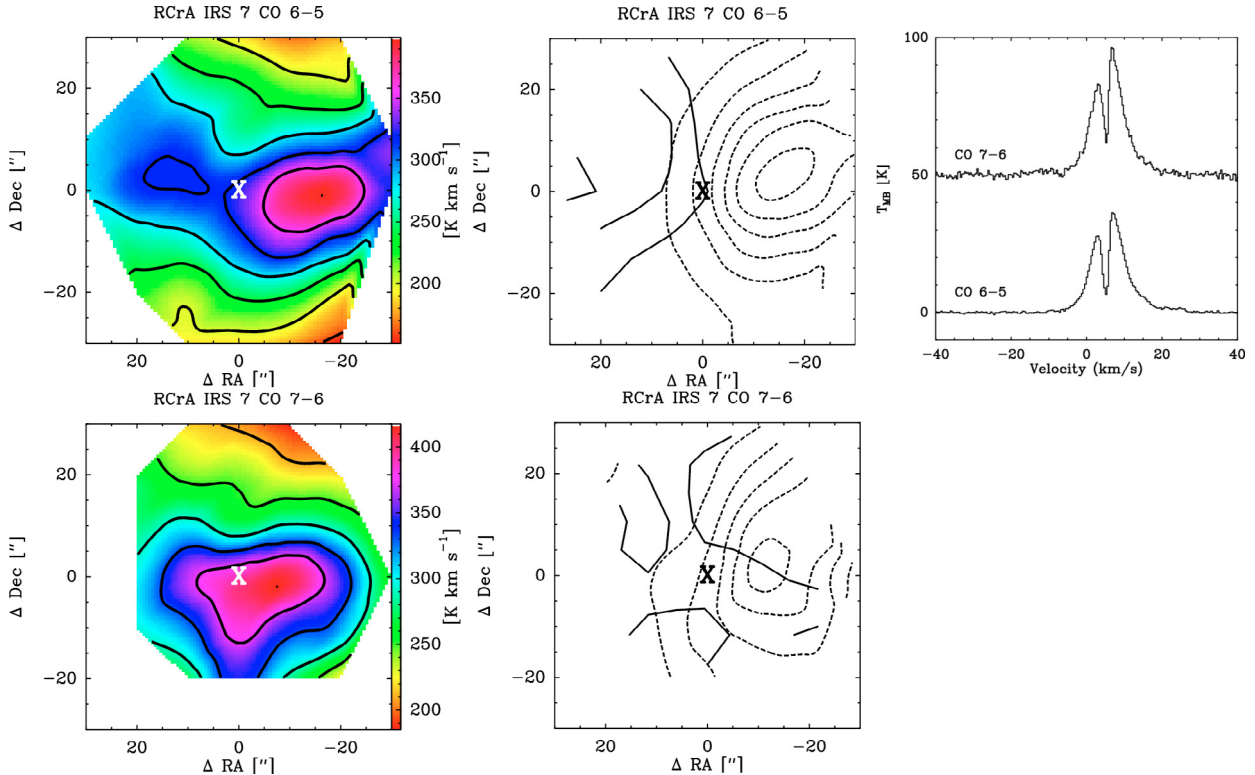


**Fig. 8.** Maps of CO 6–5 (top row) and CO 7–6 (bottom row) of RCRA IRS 7a. The left-most image shows the total integrated intensity over the line. The middle figures show the outflow contributions from the red (dashed lines) and blue (solid lines) outflow. Contours are in increasing levels of  $10 \text{ K km s}^{-1}$  for both transitions. The outflow contributions are calculated by only including emission greater or smaller than  $\pm 8 \text{ km s}^{-1}$  from the central velocity. The right-most image at the top row shows the  $^{12}\text{CO}$  spectra at the central position.

$^{12}\text{CO}$  6–5 and 7–6 was detected at the central position of all sources, ranging from  $20.8 \text{ K km s}^{-1}$  ( $T_{\text{peak}} = 7.8 \text{ K}$ ) for Ced 110 IRS 4 for CO 6–5 to  $407.6 \text{ K km s}^{-1}$  ( $T_{\text{peak}} = 46.3 \text{ K}$ ) for RCRA IRS 7A for the CO 7–6 line. All maps show extended emission, except for IRAS 12496-7650, which shows unresolved emission in the CO 7–6 transition. However, the scales on which extended emission is seen varies significantly, with detections at all mapped positions for RCRA IRS 7 to only 1 or 2 for IRAS 12496-7650, TMR 1 and Ced 110 IRS 4. All sources except RCRA IRS 7 and NGC 1333 IRAS 2 show spectra with a single peak over the entire map, while the latter two have spectra that are self-absorbed.

Figures 9 to 12 clearly identify the variation of the line profiles across the maps, especially when outflowing gas is present, such as in the maps of NGC 1333 IRAS 2, BHR 71, HH 46 and RCRA IRS 7. The sources for which little to no shocked emission is seen do show spatially resolved CO 6–5 and 7–6 emission, but always quiescent narrow emission located close to the central pixel.

### 3.2. Outflow emission

From the outflow maps in Figs. 1 to 8, it can be concluded that the contributions from shocks within the bipolar outflows to the warm gas differ greatly from source to source. RCRA IRS 7, NGC 1333 IRAS 2, HH 46, and BHR 71 produce spatially resolved flows, but TMR 1, L 1551 IRS 5, IRAS 12496-7650 and Ced 110 IRS 4 do not have warm shocked gas that results in broad high- $J$  CO in any of the off-positions. Small shocks on the source position are seen, but are generally weak. For all sources in the sample, outflow emission has been detected in low ( $J_{\text{up}} \leq 3$ ) excitation CO lines, although such flows have large differences in spatial scales, ranging from tens of arcminutes to the central twenty arcseconds (e.g. Moriarty-Schieven & Snell 1988; Fridlund et al. 1989; Cabrit & Bertout 1992; Bachiller et al. 1994; Bourke et al. 1997; Hogerheijde et al. 1998; Parise et al. 2006; van Kempen et al. 2009, submitted). Table 3 gives the integrated intensities of the CO emission at selected off-positions for the outflowing gas.

### 3.3. Isotopologue observations at the central position

For HH 46, transitions of  $^{13}\text{CO}$   $J = 6-5$  and  $8-7$  and  $\text{C}^{18}\text{O}$   $J = 6-5$  as well as [C I] 2–1 were observed (see Table 1 and 2). TMR 1, Ced 110 IRS 4, IRAS 12496-7650 and BHR 71 were observed in  $^{13}\text{CO}$  6–5 and [C I] 2–1. The results at the central position can be found in Fig. 1 to 8, as well as Table 4. All  $^{13}\text{CO}$  6–5 spectra can be fitted with single Gaussians. However, the width of the Gaussians varies with a  $FWHM$  of  $\sim 1.2 \text{ km s}^{-1}$  for HH 46 and BHR 71 to  $\sim 2.2 \text{ km s}^{-1}$  for Ced 110 IRS 4 and IRAS 12496-7650. [C I] 2–1 is detected for TMR 1, HH 46 and Ced 110 IRS 4 ( $\sim 3\sigma$ ). No line was found for IRAS 12496-7650 and BHR 71 down to a  $1\sigma$  limit of  $0.6 \text{ K}$  in  $0.7 \text{ km s}^{-1}$  bins. Integrated line strengths are on the order of  $3 \text{ K km s}^{-1}$  with widths of  $0.75 \text{ km s}^{-1}$ .  $^{13}\text{CO}$  8–7 and  $\text{C}^{18}\text{O}$  6–5 were observed towards HH 46 only, but not detected down to a  $1\sigma$  level of  $0.15$  and  $0.3$  in a  $0.7 \text{ km s}^{-1}$  channel.

### 3.4. $^{13}\text{CO}$ 6–5 and [C I] 2–1 maps

For  $^{13}\text{CO}$  6–5 and [C I] 2–1 maps were also obtained. Spectra at the central position are given in Figs. 1 to 8. Integrated intensity maps are presented in Fig. 13 ( $^{13}\text{CO}$  6–5) and Fig. 14

**Table 1.** Adopted Champ<sup>+</sup> settings.

Setting	Lines	Freq. (GHz)	Mode
A	$^{12}\text{CO}$ 6–5	691.4730	OTF/Hexa
A	$^{12}\text{CO}$ 7–6	806.6652	OTF/Hexa
B	$^{13}\text{CO}$ 6–5	661.1067	Hexa
B	[C I] 2–1	809.3435	Hexa
C	$\text{C}^{18}\text{O}$ 6–5	658.5533	Stare
C	$^{13}\text{CO}$ 8–7	881.2729	Stare

([C I] 2–1) It is seen that such observations are often dominated by centrally located unresolved emission, but not always peaked at the source. Both HH 46 and BHR 71 also show some isotopic emission associated with the outflow. For HH 46,  $^{13}\text{CO}$  6–5 is only detected off-source for the blue outflow, where part of the outflow is unobsured by cloud or envelope (Paper I).

## 4. Envelope

### 4.1. Envelope models

In order to investigate whether high- $J$  CO emission can be reproduced by a passively heated envelope, the properties of the protostellar envelopes were calculated by modelling  $850 \mu\text{m}$  continuum images, SED information and the 1-D dust radiative transfer code DUSTY described in Ivezić & Elitzur (1997) (Schöier et al. 2002; Jørgensen et al. 2002). Similar to previous studies, the so-called OH5 dust opacities were used (Ossenkopf & Henning 1994). Although NGC 1333 IRAS 2, L1551 IRS 5 and TMR 1 were included in a similar study by Jørgensen et al. (2002), new fluxes from Spitzer (e.g., Luhman et al. 2008; Gutermuth et al. 2008, see Table 2) have since come available and must be included. To constrain the models both the SED from  $\sim 50 \mu\text{m}$  to  $1.3 \text{ mm}$  and the spatial distribution of the sub-mm continuum emission at  $850 \mu\text{m}$  were used, with the exception of BHR 71 and Ced 110 IRS 4, for which no  $850 \mu\text{m}$  map is available. A normalized radial emission profile with a power law index of 1.5 for the  $850 \mu\text{m}$  emission is assumed for these two sources. The radial profiles of L 1551 IRS 5, RCRA IRS 7A, NGC 1333 IRAS 2 and TMR 1 were obtained from  $850 \mu\text{m}$  images of the processed SCUBA archive (Di Francesco et al. 2008). For HH 46 and IRAS 12496-7650, recent data from LABOCA at  $870 \mu\text{m}$  were used (see Paper I and Nefs et al. in prep.).

The parameters of the best-fitting envelope models can be found in Table 5, together with the corresponding physical parameters of the envelope. The three main parameters of DUSTY,  $Y$ , the ratio over the inner to outer radius,  $p$ , the power law exponent of the density profile  $n \propto r^{-p}$ <sup>3</sup> and  $\tau_{100 \mu\text{m}}$ , the opacity at a  $100 \mu\text{m}$ , are scaled by the  $L_{\text{bol}}$  and the distance,  $D$  given in Table 2, to get the physical properties of each source. Figure 15 shows the best-fitting model of each source of the radial profiles of the  $850 \mu\text{m}$  images and the SEDs of the entire sample.

The inner radii of the protostellar envelopes range from 5 to 35 AU corresponding to  $T_d = 250 \text{ K}$ , a limit chosen by us. Most sources also show a steep profile with all sources having  $p \geq 1.7$ , with the exception of Ced 110 IRS 4, which has a  $p = 1.4$ .

<sup>3</sup> Note that this power law index is not the same as the power law index  $p$  for the normalized  $850 \mu\text{m}$  radial emission profile.

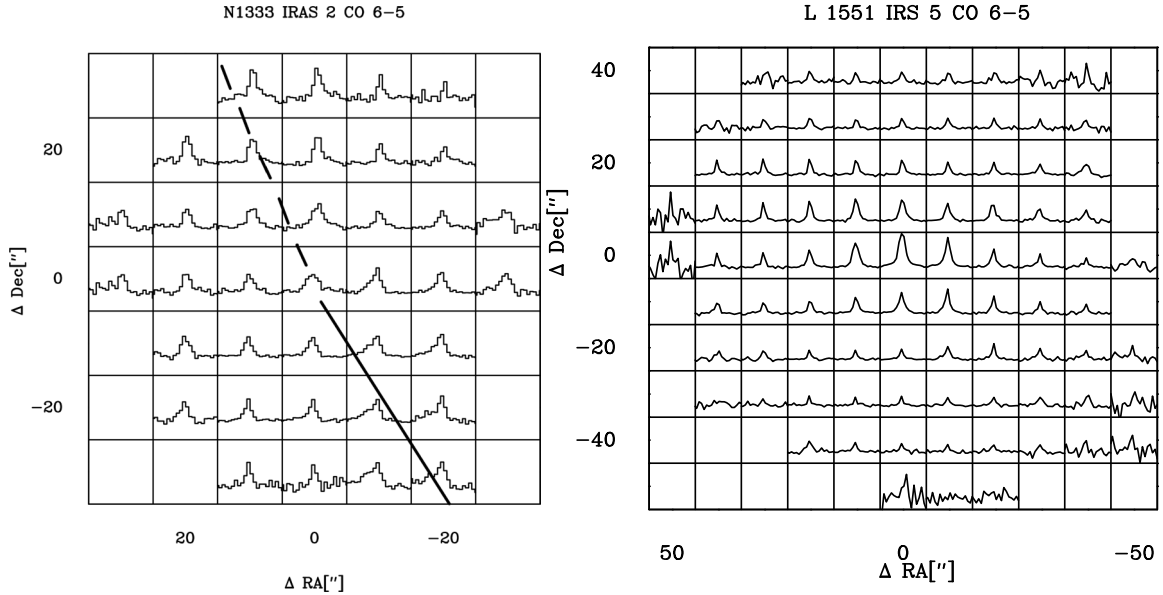


**Fig. 9.** Spectra of  $^{12}\text{CO}$  6–5 over an area of  $40'' \times 40''$  of NGC 1333 IRAS 2 (left) and L 1551 IRS 5 (right). NGC 1333 IRAS 2 was observed using the hexa mode, so the covered area is slightly smaller than that of L 1551 IRS 5 taken in OTF mode. For all spectra in both sources, horizontal axes range from  $-10$  to  $25 \text{ km s}^{-1}$  and vertical axes from  $-5$  to  $12 \text{ K}$ . For both sources, the main outflow axis of the red and blue are shown with a dashed and solid lines.

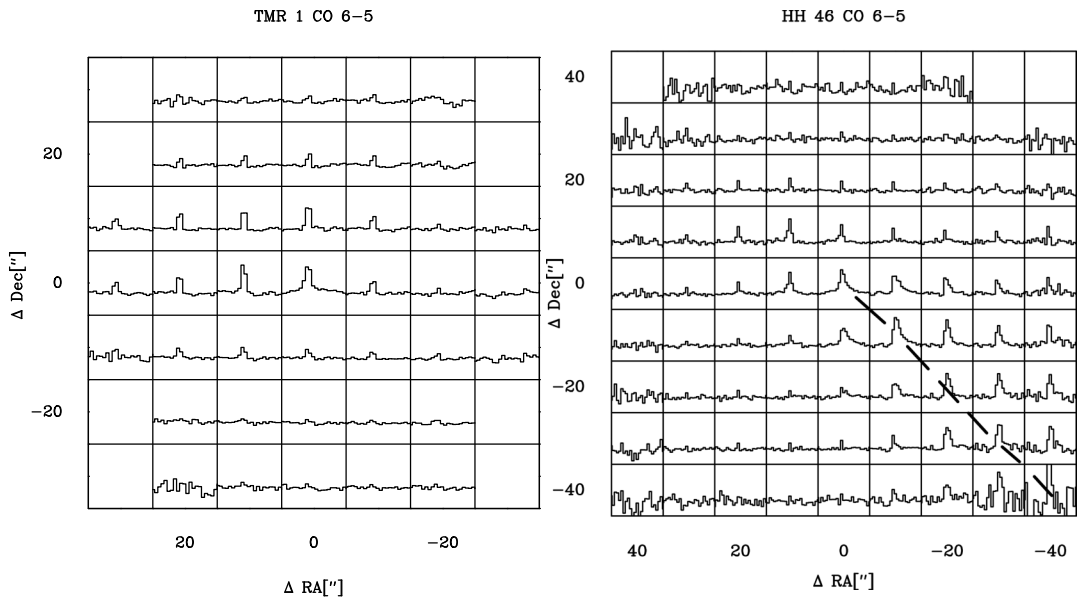


**Fig. 10.** Spectra of  $^{12}\text{CO}$  6–5 over an area of  $40'' \times 40''$  of TMR 1 (left) and HH 46 (right). TMR 1 was observed using the hexa mode, so the covered area is slightly smaller than that of HH 46 taken in OTF mode. For all spectra in both sources, the horizontal axes range from  $-10$  to  $20 \text{ km s}^{-1}$  with vertical axes from  $-5$  to  $12 \text{ K}$ . For HH 46, the red outflow axis is shown with a dashed line.

#### 4.2. CO emission within protostellar envelopes

Using the best-fit envelope temperature and density structure derived from the dust emission, the CO intensities and line profiles from the protostellar envelopes were in turn simulated with the self-consistent 1D molecular line radiative transfer code RATRAN (Hogerheijde & van der Tak 2000) using data files of the LAMDA database (Schöier et al. 2005). CO abundances with respect to H<sub>2</sub> are taken from Jørgensen et al. (2005). A “drop” abundance with  $X_0 = 2.7 \times 10^{-4}$  and  $X_d = 10^{-5}$  is adopted. This “drop” abundance profile describes a warm ( $T > T_{\text{freeze}}$ ) inner region with a high abundance  $X_0$  and a region in which  $T < T_{\text{freeze}}$  and  $n > n_{\text{de}}$  where CO is frozen out to a low abundance  $X_d$ . In the outer region ( $n < n_{\text{de}}$ ), the abundance is again

high at  $X_0$  because freeze-out timescales become longer than the typical life-times of protostars. In our models,  $T_{\text{freeze}} = 30 \text{ K}$  and  $n_{\text{de}} = 10^5 \text{ cm}^{-3}$  are adopted, following the conclusions of Jørgensen et al. (2005). There, the derived abundances are based upon the emission of low-excitation optically thin lines such as C<sup>18</sup>O lines (both 2–1 and 3–2, 1–0 is often dominated by the very cold cloud material) and C<sup>17</sup>O. Paper I showed that contrary to the low- $J$  CO lines there is little difference between “jump” and “drop” abundances for the emission in high- $J$  transitions. A static velocity field is assumed with a turbulent width of  $1 \text{ km s}^{-1}$ . Due to the static nature of the velocity field, excessive self-absorption is seen in line profiles of CO lines up to the 8–7 transition. The total area of a Gaussian fitted to the line wings

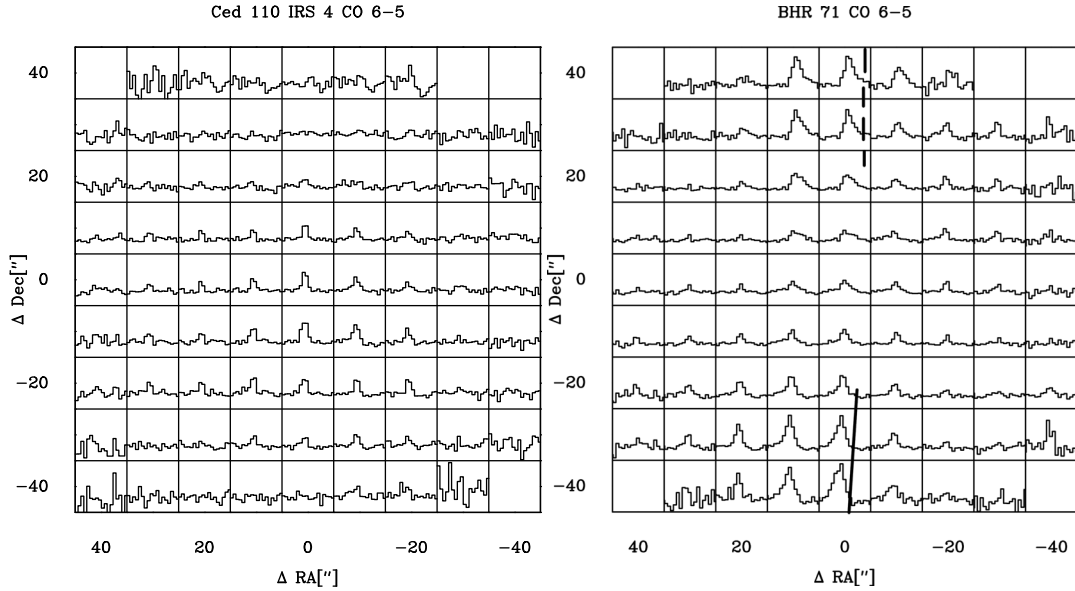


**Fig. 11.** Spectra of  $^{12}\text{CO}$  6–5 over an area of  $40'' \times 40''$  of Ced 110 IRS 4 (left) and BHR 71 (right). For Ced 110 IRS 4, the horizontal axes are  $-10$  to  $25 \text{ km s}^{-1}$  with vertical axes from  $-4$  to  $10 \text{ K}$ . For BHR 71, horizontal axes are  $-20$  to  $10 \text{ km s}^{-1}$  with vertical axes  $-5$  to  $15 \text{ K}$ . For BHR 71, the main outflow axis of the red and blue are shown with a *dashed* and *solid* lines.

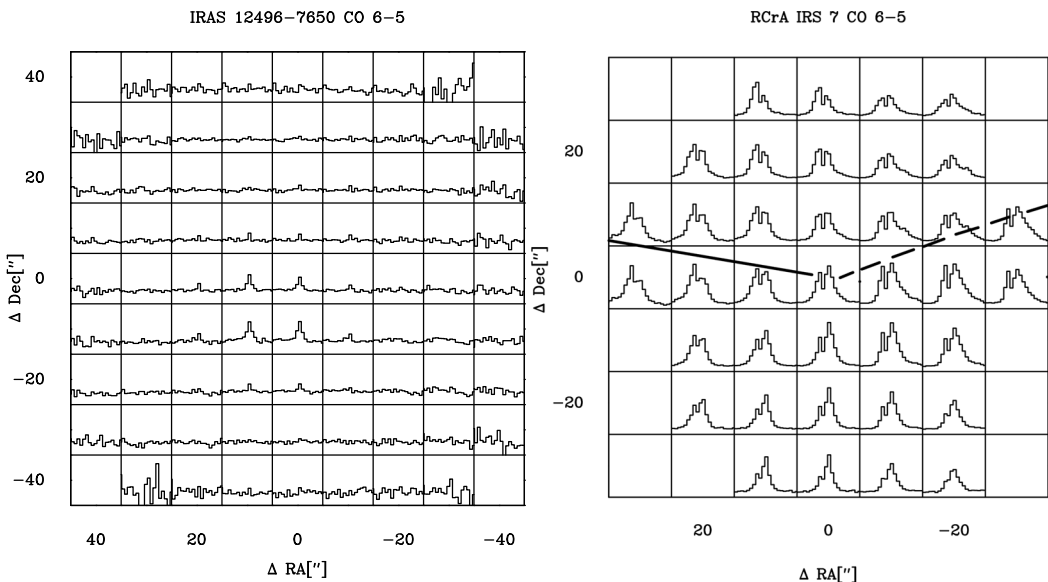


**Fig. 12.** Spectra of  $^{12}\text{CO}$  6–5 over an area of  $40'' \times 40''$  of IRAS 12496-7650 (left) and RCRA IRS 7A (right). RCRA IRS 7A was observed using the hexa mode, so the covered area is slightly smaller than that of IRAS 12496-7650 taken in OTF mode. For all spectra, the horizontal axes are  $-15$  to  $15 \text{ km s}^{-1}$  with vertical axes from  $-5$  to  $15 \text{ K}$  for IRAS 12496-7650 and from  $-10$  to  $25 \text{ km s}^{-1}$  and  $-5$  to  $50 \text{ K}$  for RCRA IRS 7. For RCRA IRS 7, the main outflow axis of the red and blue lobes are shown with a *dashed* and *solid* lines.

is used in those cases to derive an upper limit. This is a very strict limit as the true CO emission associated with the envelope is best fitted by a infall velocity (Schöier et al. 2002), producing integrated intensities between the two limits. However, Schöier et al. (2002) show that the envelope emission modelled with an infall velocity is in the worst case only a factor 2 greater than the intensity derived from the static envelope. The lower limit is derived from the actual modelled integrated intensity with the static velocity field.

Figure 16 shows the resulting integrated intensities produced by the model protostellar envelopes of all CO lines from  $J = 1$ – $0$  up to  $J = 19$ – $18$ . The data for all transitions were convolved with a  $10''$  beam used for CHAMP<sup>+</sup>, except the three lowest transitions, which are convolved with a beam of  $20''$ . Such beams are

typical for single-dish submillimeter telescopes.  $10''$  will also be the approximate beam for several transitions covered by the PACS and HIFI (Band 6 and 7) instruments on Herschel at the higher frequencies. Overplotted are the observed line strengths from various CO lines of different studies, including the far-IR high- $J$  CO lines of Giannini et al. (1999) and Giannini et al. (2001), assuming that all flux observed by the ISO-LWS in its  $80''$  beam originates in a  $10''$  region. See Table 2 for the references used.

The low- $J$  CO emission can often be completely reproduced by the envelope models, as it is dominated by the colder gas in the outer regions of the envelopes. For HH 46, Ced 110 IRS 4 and RCRA IRS 7, the observed quiescent emission in the CO 6–5 and 7–6 lines is clearly brighter by a factor of 3–5 than the

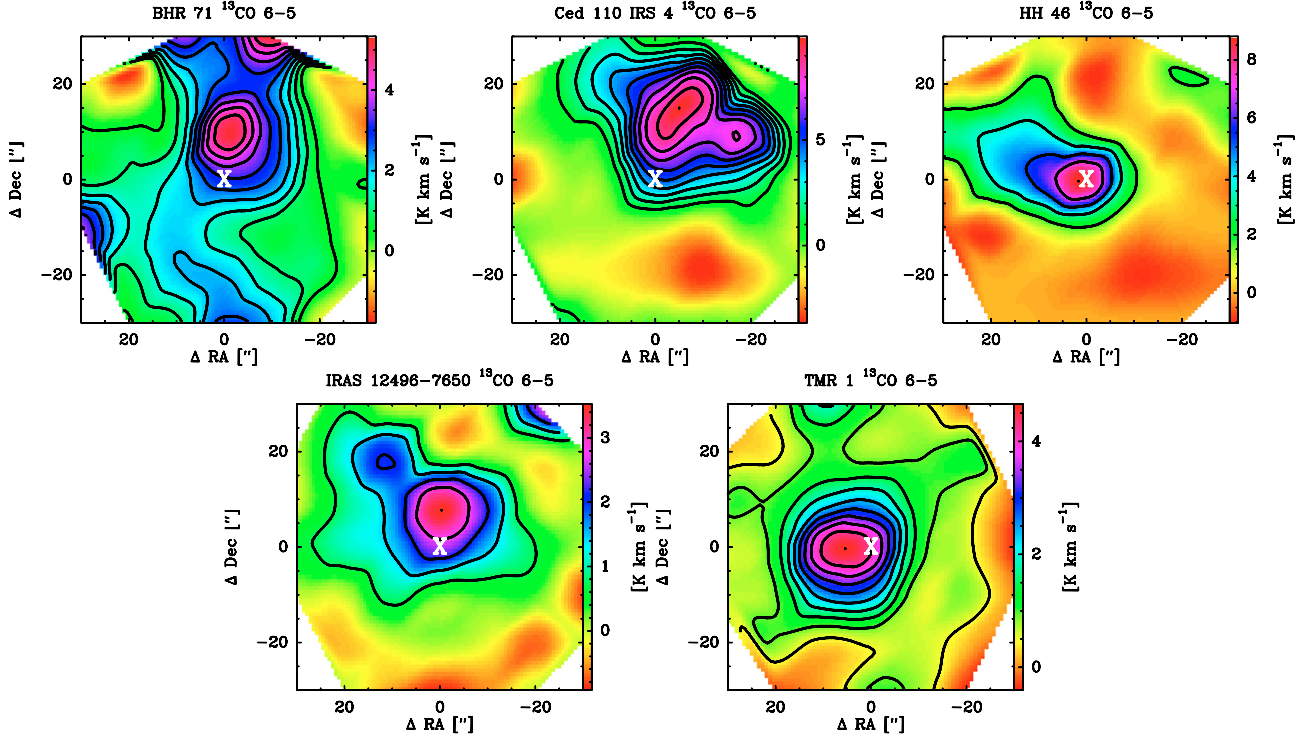


**Fig. 13.**  $^{13}\text{CO}$  6–5 integrated intensity maps of BHR 71 (*upper left*), Ced 110 IRS 4 (*upper middle*), HH 46 (*upper right*), IRAS 12496–7650 (*lower left*) and TMR 1 (*lower middle*).

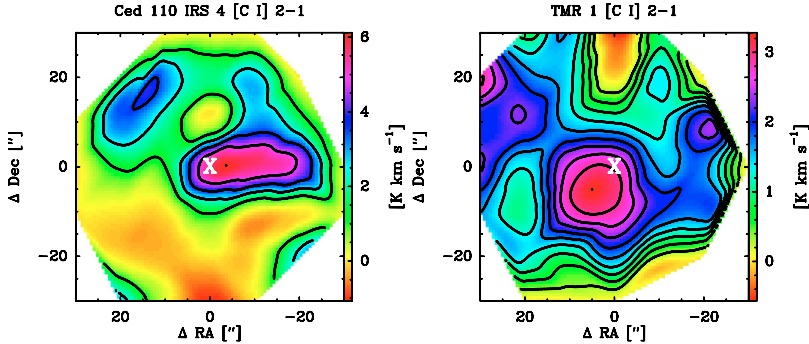


**Fig. 14.** [C I] 2–1 integrated intensity maps of Ced 110 IRS 4 (*left*) and TMR 1 (*right*). Note that the TMR 1 data suffer from a de-rotation problem in the calibrator data and are subject to change.

modelled envelope emission, even for the  $^{13}\text{CO}$  6–5 lines (see Table 6).

For RCrA IRS 7, the difference is almost an order magnitude. Deep  $\text{C}^{18}\text{O}$  6–5 spectra are needed to fully pin down the envelope models. In Paper I, the quiescent CO 6–5 and 7–6 emission of HH 46 was attributed to “photon heating” (Spaans et al. 1995), both by UV from the accretion disk and shocks inside the outflow cavity. Figure 16 clearly shows that this method of heating likely applies to other sources.

In contrast, the envelopes of both IRAS 12496–7650 and L 1551 IRS 5 can account for all the emission detected in the  $^{12}\text{CO}$  6–5 and 7–6 lines. Giannini et al. (1999) and Giannini et al. (2001) report emission of high- $J$  CO (14–13 to 19–18) lines at far-IR of NGC 1333 IRAS 2, IRAS 12496–7650 and RCrA. For RCrA, RCrA IRS 7 is within the beam, but the emission is probably dominated by emission from RCrA itself. Fluxes in excess of  $10^{-20}$  W cm $^{-2}$  are seen for IRAS 12496–7650. They assumed that the flux originates within the central 3'' (~400 AU). It is very clear from Fig. 16 that such observed emission cannot be

produced by a passively heated envelope. A more likely explanation is that the CO emission detected with ISO-LWS is either located outside the inner 10'' as is the likely case for IRAS 12496–7650 (see van Kempen et al. 2006) or associated with an energetic outflow.

## 5. Outflows

### 5.1. Shocks

Bachiller & Tafalla (1999) propose an evolutionary sequence of outflows around low-mass protostars, with young deeply embedded YSOs (Class 0) producing highly collimated and energetic outflows, and with more evolved embedded YSOs (Class I) producing outflows which show less energetic shocks and a wider opening angle (Arce et al. 2007, see also). Observations of the shocked  $^{12}\text{CO}$  6–5 and 7–6 gas in the outflow directions confirm the scenario that the shocks within the vicinity of the protostar grow weaker in energy over time. The Class 0 sources (NGC 1333 IRAS 2, BHR 71 and RCrA IRS 7) all show shocked

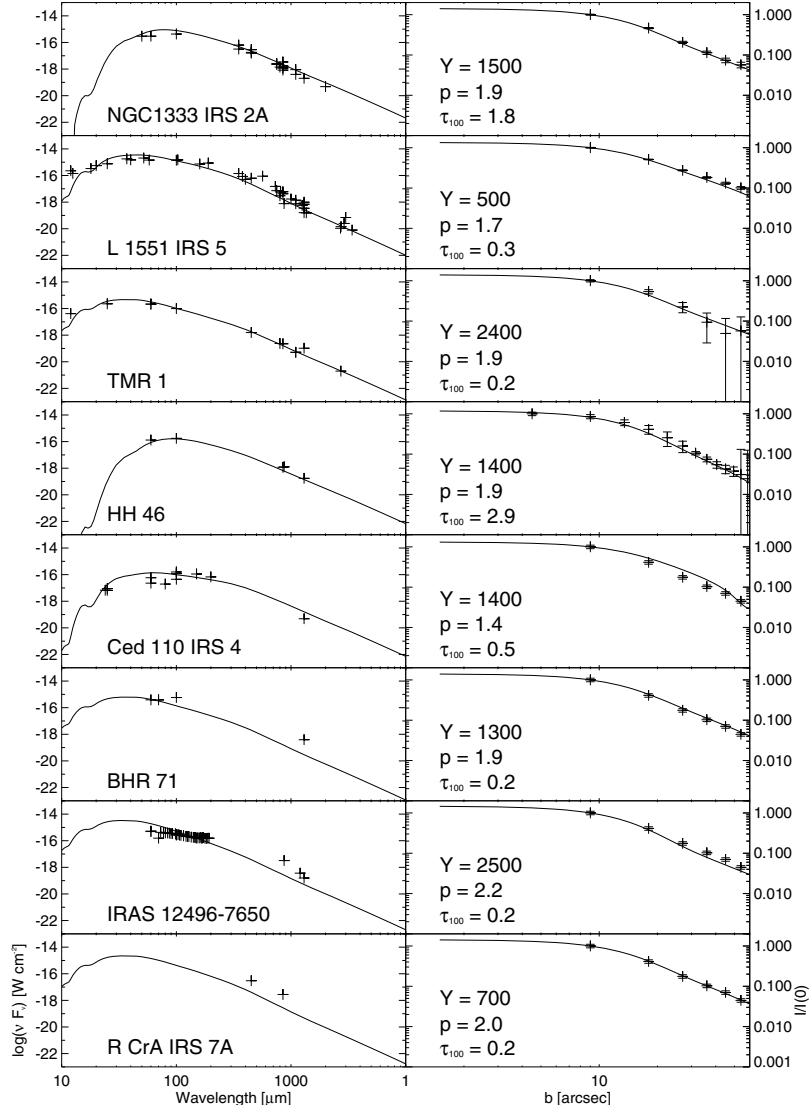


**Fig. 15.** The SEDs and radial profiles at 850  $\mu\text{m}$  of the sample. Overplotted is the best-fitting envelope model. For Ced 110 IRS 4 and BHR 71, the model spatial 850  $\mu\text{m}$  profile of 1.5 is plotted since data are lacking. Note that this power law index of 1.5 does not equal the power law index  $p$ .

warm gas in their CO 6–5 and 7–6 lines, in both blue- and red-shifted outflow. Of the Class I sources, only HH 46 shows shocked gas in its red-shifted outflow. L 1551 IRS 5, one of the most-studied molecular outflows (Moriarty-Schieven & Snell 1988; Bachiller et al. 1994), shows little emission in the high-J lines associated with outflow shocks. Although several spectra do show a small outflow wing, the integrated emission in the wings is not higher than a few  $\sigma$ . All other Class I flows show no sign of shocked warm gas. HH 46 and L 1551 IRS 5, even though classified as Class I, have massive envelopes of a few  $M_\odot$ , more characteristic of Class 0 (Jørgensen et al. 2002). L 1551 IRS 5 is believed to be older and to consist of several successive ejection events (Bachiller et al. 1994; White et al. 2000).

Figure 17 shows the maximum outflow velocities of the  $^{12}\text{CO}$  6–5 and 3–2 lines vs. the bolometric temperature, envelope mass and outflow force. A clear absence of warm high-velocity material is seen for sources with a higher bolometric temperature. Only the cold outflow of IRAS 12496-7650 is seen at higher  $T_{\text{bol}}$  (van Kempen et al. 2006). Similarly, there is also a clear relation between the mean outflow force of both red and blue outflow lobes, and the maximum velocity seen in both  $^{12}\text{CO}$  3–2 and  $^{12}\text{CO}$  6–5 emission. Outflow forces are derived

from the spatial scales and velocities of low-excitation CO line emission (1–0, 2–1 and 3–2) (Cabrit & Bertout 1992; Bourke et al. 1997; Hogerheijde et al. 1998, Paper I; van Kempen et al. 2009, submitted)

## 5.2. Temperatures of the swept-up gas

The excitation temperature of the outflowing swept-up gas can be derived from the ratios of different CO line wings. As an example, Fig. 18 shows the CO 3–2 data from van Kempen et al. (2009) submitted and Paper I and CO 6–5 data from this paper overplotted on the same scales for a few sources. The CO 6–5 data have not been binned to the larger CO 3–2 beam, so the comparison assumes similar volume filling factors of the shocked gas; for HH 46 in Paper I it has been checked that rebinning gives similar results within the uncertainties. If the density is known this excitation temperature can be related to the kinetic temperature using the diagnostic plots produced by the RADEX radiative transfer code (van der Tak et al. 2007).

As can be seen from the temperature analysis of HH 46 (Paper I), there are many uncertainties, leading to error bars as large as 50 K on the inferred temperatures. The ratios depend on

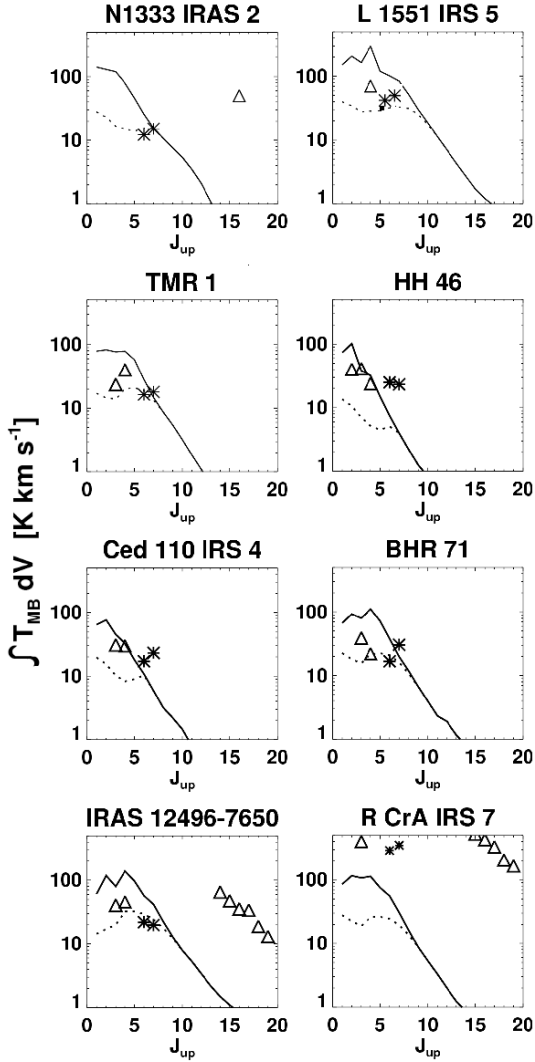


**Fig. 16.** The contribution of the envelope to CO lines at the source position with  $J_{\text{up}}$  ranging from 1 to 19. Integrated emission is shown with dashed and solid lines. Dashed lines are modelled lines which show excessive self-absorption. Solid lines represent Gaussian fitted to the line wings of the envelope model and thus represent the strict upper limit to the CO line emission from the protostellar envelope. Beam-sizes were taken to be  $10''$  for all transitions except for  $J_{\text{up}} \leq 3$ , for which a beam of  $20''$  was used. Stars indicate the integrated quiescent emission of the lines observed with CHAMP<sup>+</sup> from Table 3 at the source position, corrected for red- and blue-shifted emission, while triangles are literature data (see Table 2).

the velocity, the optical depth of the line wings and the ambient density at different distances from the source. For HH 46, a drop in temperature was observed if the density remains constant, but it is more plausible that the density is lower at larger radii which will result in a constant kinetic temperature with distance.

Table 7 gives the median temperatures using the extreme velocities of the line wings with intensities  $>3\sigma$ , assuming the line wings are optically thin and with an ambient cloud density of  $10^4 \text{ cm}^{-3}$ . CO 3–2 spectra can be found in Hogerheijde et al. (1998) (TMR 1, L 1551 IRS 5), Knee & Sandell (2000) (NGC 1333 IRAS 2), Parise et al. (2006) (BHR 71), van Kempen et al. (2006) (IRAS 12496-7650), van Kempen et al. (2009, submitted) (RCrA IRS 7, Ced 110 IRS 4) and Paper I (HH 46).

The main error on these temperature estimates is the optical depth in the outflow wings. Deep  $^{13}\text{CO}$  3–2 observations show

that outflows can be optically thick. Hogerheijde et al. (1998) find optical depths in the  $^{12}\text{CO}$  3–2 line wings,  $\tau_{\text{wing}}$ , on the order of 10, while in Paper I  $\tau_{\text{wing}} = 1\text{--}1.8$  is found for HH 46. Even if the optical depths are assumed to be similar in CO 3–2 and CO 6–5, kinetic temperatures can be almost 50% lower than those given in Table 7.

For a more thorough discussion about the density of the surrounding envelope and cloud material, see Paper I. Our choice of the density of  $10^4 \text{ cm}^{-3}$  is based on the typical densities found in model envelopes of Jørgensen et al. (2002) at distances of a few thousand AU, corresponding to the 10 K radius where the envelope merges with the surrounding molecular cloud. Higher densities will produce lower outflow temperatures (see Paper I for more extensive discussion).

A theoretical study by Hatchell et al. (1999) using a jet-driven bow shock model suggests that the kinetic temperatures of molecular outflows are typically of order of 50–150 K along the axis and rising toward the location of the bow shock, with overall values increasing with higher jet velocities. The temperatures found in Table 7 agree well with these predicted temperatures. For several outflows, e.g., IRAS 12496-7650 (blue) or Ced 110 IRS 4 (red), temperatures are significantly lower, however. The lowest outflow temperatures are found for the flows of L 1551 IRS 5, where CO 4–3/6–5 ratios are on the order of 8 or higher. At an assumed density of  $10^4 \text{ cm}^{-3}$ , this corresponds to kinetic temperatures of 50 K and lower. If both line wings are optically thin, densities must be lower than  $10^3 \text{ cm}^{-3}$  to produce temperatures of  $\sim 100$  K, observed for other flows.

## 6. Heating processes in the molecular outflow and protostellar envelope

As discussed in Sect. 4, several sources show quiescent, narrow  $^{12}\text{CO}$  6–5 and 7–6 emission that is more intense than can be produced by an envelope model. Moreover, strong narrow high- $J$  CO emission is observed off-source along outflow axes for most sources. In Paper I, we proposed that for HH 46 the quiescent narrow  $^{12}\text{CO}$  6–5 and 7–6 line emission originates within the outflow cavity walls heated to 250–400 K by an enhancement factor  $G_0$  with respect to the standard interstellar radiation field of a few hundred. The UV photons can be created by jet shocks in the outflow cavities as well as in the disk-star accretion boundary layer near the central protostar. This heating method was first proposed by Spaans et al. (1995), but extended by Paper I to both the inner envelope as well as the outflow cavity walls much further from the central star. The data presented in this paper show that photon heating is present in other protostars as well, especially in outflow cavities. Even in sources with little to no outflow, such as Ced 110 IRS 4, relatively strong narrow  $^{12}\text{CO}$  6–5 and 7–6 lines are seen at positions not associated with the central protostar, see Fig. 16. The presence of significant radiative “feedback” from the protostar on its surroundings may have consequences for the collapse of the envelope, limiting the accretion rate and mass of the star and suppressing disk fragmentation (e.g., Offner et al. 2009).

The origin of such quiescent high- $J$  CO emission at the source velocity is physically different from both the thermal emission of the protostellar envelope (see Sect. 6.4), emission from shocks present at the working surfaces of outflows (Reipurth & Raga 1999; Raga et al. 2007).

Slow ( $v_s = 5\text{--}10 \text{ km s}^{-1}$ ) C-shocks may produce similar quiescent levels of CO 6–5 and 7–6 emission in outflows (Draine & Roberge 1984; Spaans et al. 1995). However, the presence of

**Table 2.** The sample of sources observed with CHAMP+.

Source	RA (J2000)	Dec (J2000)	D (pc)	$L_{\text{bol}}$ ( $L_{\odot}$ )	$T_{\text{bol}}$ (K)	Class
NGC 1333 IRS 2	03:28:55.2	+31:14:35	250	12.7	62	0
L1551 IRS 5	04:31:34.1	+18:08:05.0	160	20	75	1
TMR 1	04:39:13.7	+25:53:21	140	3.1	133	1
HH 46	08:25:43.8	-51:00:35.6	450	16	102	1
Ced 110 IRS 4	11:06:47.0	-77:22:32.4	130	0.8	55	1
BHR 71	12:01:36.3	-65:08:44	200	11	60	0
IRAS 12496-7650	12:53:17.2	-77:07:10.6	250	24	326 <sup>b</sup>	1
RCrA IRS 7A <sup>c</sup>	19:01:55.2	-36:57:21.0	170	—	—	0
	Sett. <sup>a</sup>	Ref. Cont.		Ref. CO		
NGC 1333 IRS 2	A	1, 2, 3, 4, 5, 6, 7		vii		
L1551 IRS 5	A	2, 8, 9, 10, 11, 12		i		
TMR 1	AB	13, 14, 15, 16		i		
HH 46	ABC	1, 17, 18		ii, iii		
Ced 110 IRS 4	AB	7, 19, 20, 21, 22		iii, iv		
BHR 71	AB	17, 23, 24, 25		v		
IRAS 12496-7650	AB	26, this work		iii, viii		
RCrA IRS 7A <sup>c</sup>	A	1, 7, 27, 28		iii, viii		

<sup>a</sup> Observed settings with CHAMP+. See Table 1.

<sup>b</sup> IRAS 12496-7650 is likely to be viewed face-on and thus has strong IR emission and a high  $T_{\text{bol}}$ . See van Kempen et al. (2009, submitted).

<sup>c</sup> RCrA IRS 7 is a binary. Pointing was chosen to be on RCrA IRS 7A, believed to be the main embedded source, following results from van Kempen et al. (2009, submitted) and Groppi et al. (2007). RCrA IRS 7B is located 15'' to the east. At mid- and far-IR wavelengths, the source is heavily confused with RCrA. Therefore, no reliable  $T_{\text{bol}}$  and  $L_{\text{bol}}$  could be derived.

Continuum References: 1: Di Francesco et al. (2008) 2: Motte & André (2001) 3: Gutermuth et al. (2008) 4: Enoch et al. (2006) 5: Hatchell et al. (2007) 6: Sandell & Knee (2001) 7: Froebrich (2005) 8: Chandler & Richer (2000) 9: Reipurth et al. (2002) 10: Osorio et al. (2003) 11: Liu et al. (1996) 12: Butner et al. (1991) 13: Kenyon et al. (1994) 14: Hogerheijde et al. (1999) 15: Furlan et al. (2008) 16: Terebey et al. (1993) 17: Henning & Launhardt (1998) 18: van Kempen et al. (2009) 19: Reipurth et al. (1993) 20: Luhman et al. (2008) 21: Lehtinen et al. (2001) 22: Lehtinen et al. (2003) 23: Evans et al. (2007) 24: Bourke et al. (1997) 25: Bourke (2001) 26: Henning et al. (1993) 27: Nutter et al. (2005) 28: Groppi et al. (2007)

CO references: i: Hogerheijde et al. (1998), ii: van Kempen et al. (2009, submitted), iii: Paper I, iv: Hiramatsu et al. (2007), v: Parise et al. (2006), vi: Knee & Sandell (2000), vii: Giannini et al. (2001), viii: Giannini et al. (1999).

quiescent  $^{12}\text{CO}$  6–5 and 7–6 emission in the envelopes of TMR 1 and Ced 110 IRS 4, both of which show little to no spatially resolved outflow emission in the CO 3–2 line (Hogerheijde et al. 1998; van Kempen et al. submitted), is more easily explained with the photon heating scenario than with slow C-shocks. In addition, the narrow line widths for other sources argue against this scenario.

### 6.1. Envelope and outflow of BHR 71

The proposed model that photon heating takes place both in the outflow cavities and the inner envelope is clearly illustrated by the observations of BHR 71. At the north and south position of the outflow, shocked gas is clearly detected, but almost no shocked gas is seen near the central star. Quiescent gas with  $\Delta V = 1.5 \text{ km s}^{-1}$  is observed both within the inner envelope and along the outflow. In the  $^{12}\text{CO}$  7–6 map, the photon heating in the envelope can be strongly identified by the central contour. BHR 71 is the only source for which the quiescent emission at the outflow position is (much) brighter than that seen at the position of the envelope. It is likely that strong shocks producing copious UV are present in the main outflow. This outflow (Bourke et al. 1997) is clearly detected at the edges of the map, but the secondary weaker outflow, associated with the IRS2 position, as seen by Parise et al. (2006) is not detected down to the noise levels. Shocked CO 6–5 and 7–6 emission is also only seen at relatively low levels in the inner 20'' and strongly increases at 40'' away from the source for both outflows.

### 6.2. The “fossil” outflow of L 1551 IRS 5

The outflow of L 1551 IRS 5 has been considered an example of an older outflow, due to its large size (Moriarty-Schieven & Snell 1988; Fridlund et al. 1989), large opening angle (Bachiller et al. 1994) and other submillimeter properties (Cabrit & Bertout 1992; Bachiller et al. 1994; Hogerheijde et al. 1998). White et al. (2000) constructed a detailed model from a wide variety of space- and ground-based IR continuum and spectroscopic observations, including a wide opening angle of the outflow ( $\sim 50^\circ$ ) and low densities inside the cavity. This view is clearly confirmed by the low derived temperatures of 40 to 50 K of the shocked gas, which is much cooler than in other sources. Little high- $J$  CO emission is seen at the off-positions, and the maps are dominated by the emission of the central source. Comparison of the peak temperatures of CO 4–3 (Hogerheijde et al. 1998), 6–5 and 7–6 shows that  $T_{\text{peak}}$  at high- $J$  transitions is similar to that at low- $J$  CO transitions. This suggest that even though the outflow is present, the density in the surrounding cloud must be quite low.

### 6.3. The PDR of RCrA IRS 7

The lines of RCrA IRS 7 are an order of magnitude stronger than those of equivalent sources in different clouds. Even at off-positions at the edge of the observed area, integrated intensities larger than  $300 \text{ K km s}^{-1}$  are seen. Even with the high luminosity of  $\sim 20\text{--}30 L_{\odot}$ , these integrated intensities cannot originate from heating by RCrA IRS 7 itself. A likely

**Table 3.** Properties of the  $^{12}\text{CO}$  lines<sup>a</sup>.

Source	Offpos.	$V_{\text{LSR}}$	CO 6–5					
			$\int T_{\text{MB}} \text{d}V$ K km s <sup>-1</sup>	$T_{\text{peak}}$ K	red K km s <sup>-1</sup>	blue K km s <sup>-1</sup>	rms <sup>b</sup> K	
NGC 1333 IRS 2	0, 0	7.0	34.3	6.8	8.9	13.2	0.6	
	0, 20	7.0	43.7	9.8	20.0	—	0.6	
	-20, -20	7.0	36.3	7.6	2.2	11.0	0.7	
L 1551 IRS 5	0, 0	6.8	39.5	7.8	13.8	10.7	0.3	
TMR 1	0, 0	4.5	23.4	8.1	2.5	5.2	0.3	
HH 46	0, 0	4.4	45.3	9.3	10.6	10.4	0.3	
	-20, -20	4.4	33.4	9.1	11.1	—	0.5	
	0, 0	3.5	20.8	7.8	—	4.8	0.4	
BHR 71	0, 0	-4.5	38.6	5.2	9.1	12.7	0.4	
	10, -40	-4.5	96.3	16.5	—	68.1	1.0	
	0, 40	-4.5	75.8	13.0	41.5	—	1.0	
IRAS 12496-7650	0, 0	1.8	22.1	5.9	—	—	0.5	
RCrA IRS 7A <sup>c</sup>	0, 0	5.7	337.9	36.3	33.6	10.9	0.3	
Source			CO 7–6					
NGC 1333 IRS 2	Offpos.	$V_{\text{LSR}}$	$\int T_{\text{MB}} \text{d}V$ K km s <sup>-1</sup>	$T_{\text{peak}}$ K	red K km s <sup>-1</sup>	blue K km s <sup>-1</sup>	rms <sup>b</sup> K	
			7.0	29.2	6.3	8.8	5.2	1.7
			7.0	65.8	10.1	27.8	5.2	1.7
L 1551 IRS 5	-20, -20	7.0	—	—	—	—	3.5	
			6.5	52.9	9.2	18.9	11.6	0.4
			4.5	19.8	10.1	1.5	1.8	0.7
HH 46	0, 0	4.4	34.2	8.4	—	9.9	0.8	
			4.4	29.8	6.2	15.7	—	1.0
			3.5	23.1	7.1	—	—	1.0
BHR 71	0, 0	-4.5	36.6	4.4	5.4	—	0.7	
			-4.5	41.5	7.0	5.6	17.2	2.8
			-4.5	54.7	9.1	27.0	—	3.0
IRAS 12496-7650	0, 0	1.8	19.9	6.1	—	—	1.4	
			5.7	407.6	46.3	29.0	22.2	0.7

<sup>a</sup> Red is the redshifted outflow lobe calculated from -10 to -1.5 km s<sup>-1</sup> with respect to the source velocity. Blue is the blueshifted outflow lobe calculated from +1.5 to +10 km s<sup>-1</sup> with respect to the source velocity.

<sup>b</sup>  $1\sigma$  in a 0.8 km s<sup>-1</sup> channel.

<sup>c</sup> Outflowing gas refers to emission in -20 to -8 km s<sup>-1</sup> and +8 to +20 km s<sup>-1</sup> from line center.

explanation is the proximity of the A5 star RCrA ( $L_{\text{bol}} = 130 L_{\odot}$ ) at 36'' (4500 AU). RCrA was observed by ISO-LWS, and many strong high- $J$  CO lines (CO 14–13 to 21–20) were detected in the large beam of ISO (Lorenzetti et al. 1999; Giannini et al. 1999). Models were put forward with the emission originating in relatively small ( $\sim 0.002$  pc), dense ( $> 10^6$  cm<sup>-3</sup>) and hot ( $T > 300$ –1000 K) regions (Giannini et al. 1999). However, the spatial distribution of the CO 6–5 and 7–6 seen in Fig. 8 does not agree with this hypothesis. A much more likely explanation is that RCrA itself irradiates the outer edges of the cloud and envelope around RCrA IRS 7a, creating a PDR at its surface, much like the case of intermediate mass sources in Orion (Jørgensen et al. 2006).

#### 6.4. Presence of [C I] 2–1

A limit on the amount of FUV/X-ray emission that is available to dissociate CO and H<sub>2</sub> can be derived from the presence of the [C I] 2–1. Photodissociation of CO can only occur at 912–1100 Å (van Dishoeck & Black 1988), so the absence of strong [C I] 2–1 emission in the outflow cavities of most protostars suggests that the radiation field in outflows does not produce sufficiently energetic radiation, but still heats the cavity walls to a few hundred K. This would also

limit the shock velocities to <90 km s<sup>-1</sup>, since higher shock velocities produce CO and H<sub>2</sub> dissociating photons (Neufeld & Dalgarno 1989).

[C I] is detected in the inner 10'' for HH 46, TMR 1 and Ced 110 IRS 4 at levels of 2 K km s<sup>-1</sup>. For IRAS 12496-7650 and BHR 71, no [C I] 2–1 was detected. The low emission in all sources can be accounted for by a C abundance of a few times 10<sup>-6</sup> with respect to H<sub>2</sub>. Such abundances can be maintained by low UV levels produced by cosmic ray radiation (Flower et al. 1994).

## 7. Conclusions

In this paper, we have presented the first  $^{12}\text{CO}$  6–5 and 7–6 maps of a sample of 8 low-mass protostars with a large range of luminosities, evolution and densities, as well as several isotopologue and [C I] observations. All observations have been carried out with the CHAMP<sup>+</sup> instrument. The main conclusions of this paper are:

- Warm gas, as traced by  $^{12}\text{CO}$  6–5 and 7–6, is present in all observed protostars at the central position. Three different origins of the warm gas emission are found: (i) the inner envelope heated passively by the protostellar luminosity; (ii) shocked gas in the outflow; and (iii) quiescent gas heated by

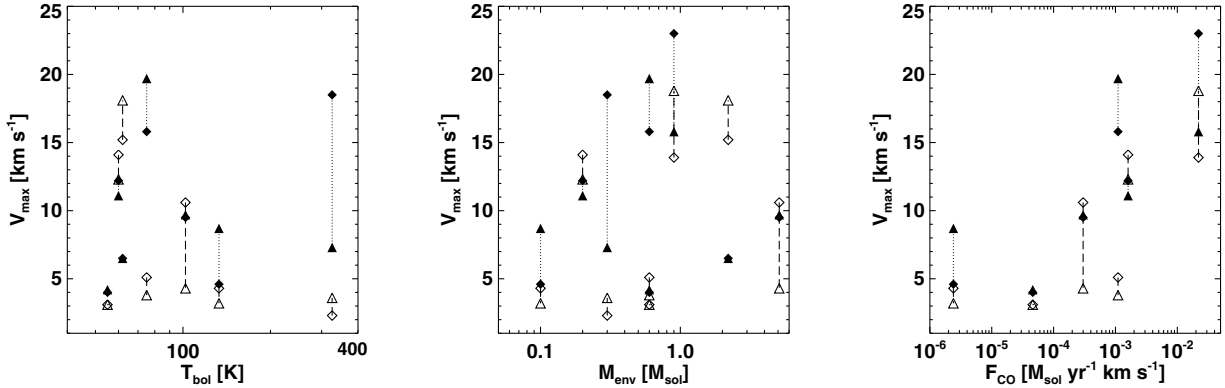


**Fig. 17.**  $V_{\max}$  of  $^{12}\text{CO}$  6–5 and 3–2 vs.  $T_{\text{bol}}$  (left), envelope mass (middle) and outflow force. Triangles represent the blue outflows and diamonds the red outflows. Open symbols are the CO 6–5 lines and filled symbols the CO 3–2 lines. Outflow force from Cabrit & Bertout (1992); Hogerheijde et al. (1998) (NGC 1333 IRAS 2, L 1551 IRS 5 and TMR 1), Bourke et al. (1997) (BHR 71) and van Kempen et al. submitted (Ced 110 IRS 4, IRAS 12496-7650, RCRA IRS 7) and van Kempen et al. (2009) (HH 46). CO 3–2 from Parise et al. (2006) (BHR 71), Hogerheijde et al. (1998) (TMR 1, L 1551 IRS 5), Knee & Sandell (2000) (NGC 1333 IRAS 2), van Kempen et al. (2006) (IRAS 12496-7650) and van Kempen et al. 2009, submitted (HH 46, RCRA IRS 7 and Ced 110 IRS 4).

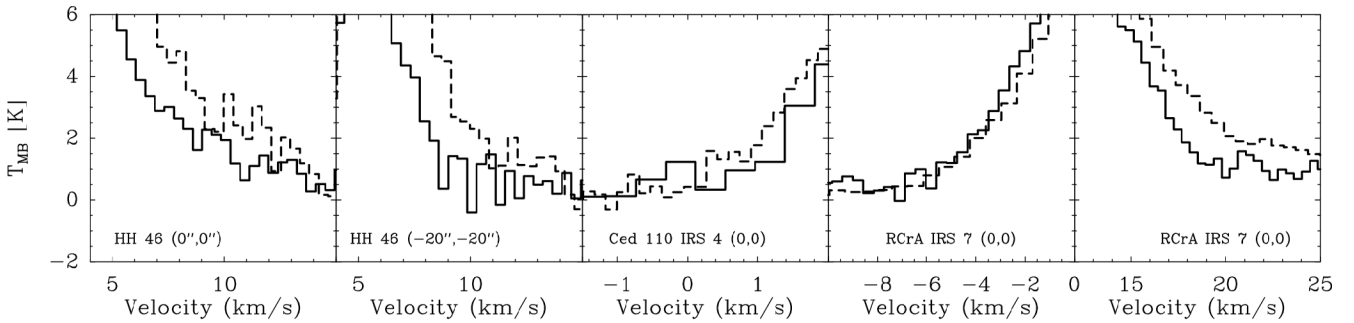


**Fig. 18.** Line wings of CO 6–5 (solid) and CO 3–2 (dashed) for HH 46 (red wing at central position and in the red outflow), Ced 110 IRS 4 (blue at the central position), RCRA IRS 7A (red and blue at the central position).

**Table 4.** CO isotopologue and [C I] properties at the source position.

Source	$^{13}\text{CO}$ 6–5			$^{13}\text{CO}$ 8–7	$\text{C}^{18}\text{O}$ 6–5	[C I] 2–1
	$\int T_{\text{MB}} dV$	$T_{\text{peak}}$	$FWHM$	$\int T_{\text{MB}} dV$	$\int T_{\text{MB}} dV$	$\int T_{\text{MB}} dV$
TMR 1	4.3	1.9	2.0	–	–	2.9
HH 46	3.9	3.1	1.5	<0.3 <sup>a</sup>	<0.15 <sup>a</sup>	2.3
Ced 110 IRS4	5.2	2.1	2.3	–	–	2.5
BHR 71	1.4	1.5	0.8	–	–	<0.6 <sup>a</sup>
IRAS 12496-7650	3.8	1.7	2.1	–	–	<0.6 <sup>a</sup>

<sup>a</sup>  $1\sigma$  level in a  $0.7 \text{ km s}^{-1}$  bin.

**Table 5.** Inferred envelope properties from the DUSTY models.

Source	$Y$	$p$	$\tau_{100}$	$R_{\text{inner}}$ (AU)	$R_{\text{outer}}$ ( $10^4$ AU)	$n_{1000 \text{ AU}}$ ( $10^4 \text{ cm}^{-3}$ )	$M_{\text{env}}(< R_{\text{outer}})$ ( $M_{\odot}$ )
RCRA IRS 7A	700	2.0	0.2	24.7	5.9	13	0.9
NGC 1333 IRAS 2	1500	1.9	1.8	31.3	1.6	140	2.2
L 1551 IRS 5	500	1.7	0.3	26.5	1.3	33	0.6
TMR 1	2400	1.9	0.2	9.5	2.3	5.4	0.1
IRAS 12496-7650	2500	2.2	0.2	35.7	8.9	8.7	0.3
HH 46	700	1.8	2.6	30.0	2.1	250	5.1
BHR 71	1300	1.9	0.2	15.6	2.0	8.5	0.2
Ced 110 IRS 4	1400	1.4	0.5	5	0.7	51	0.6

**Table 6.**  $^{13}\text{CO}$  model predictions.

Source	$\int T_{\text{MB}} dV$		$T_{\text{peak}}$	
	Mod.	Obs.	Mod.	Obs.
TMR 1	3.6	4.3	1.9	1.9
IRAS 12496-7650	7.2	3.3	3.6	1.6
HH 46	1.9	3.9	1.2	2.9
BHR 71	4.7	1.4	2.7	1.2
Ced 110 IRS 4	2.3	5.2 <sup>a</sup>	1.2	1.9

<sup>a</sup> Possible outflow contribution, see Figs. 5 and 13, estimated to be at 25% of total integrated intensity.

UV photons. This latter mechanism, as detailed in Spaans et al. (1995) and in Paper I, generally dominates the extended high- $J$  CO emission.

- Envelope models show that for HH 46 and Ced 110 IRS 4, passive heating of the envelope is insufficient to explain the observed  $^{12}\text{CO}$  6–5, 7–6 and  $^{13}\text{CO}$  6–5 lines, requiring heating of the envelope by UV photons even at the (0, 0) position.
- Photon heating of the cavity walls takes place on arcmin scales for the outflow cavities of several other Class 0 and Class I protostars, as seen at positions off-source of BHR 71, NGC 1333 IRS 2, HH 46 and L 1551 IRS 5. The necessary UV photons are created by internal jet shocks and the bow shock where the jet interacts with the ambient medium, in addition to the disk-star accretion boundary layer. The distribution of the quiescent CO 6–5 and 7–6 emission of BHR 71, with narrow emission stronger at larger distances from the source, confirms the hypothesis that UV photons necessary for the heating can originate both mechanisms. This suggests that photon heating is present in all outflows.
- The lack of [C I] 2–1 emission in the outflows constrains the production of energetic CO dissociative photons in the shocks. The observed [C I] emission at the source position can be accounted for by a low atomic C abundance that is maintained by cosmic ray induced UV photodissociation of CO.
- Shocked  $^{12}\text{CO}$  6–5 and 7–6 gas only exists in large quantities in flows of more massive sources (NGC 1333 IRS 2, BHR 71, HH 46 and RCRA IRS 7), while low-mass flows do not show much shocked gas that emits in the  $^{12}\text{CO}$  6–5 and 7–6 lines. Within the proposed model of Bachiller & Tafalla (1999), the outflows of Class I are more evolved and are driven with much less energy, producing much weaker shocks. This is also reflected in the decreasing maximum velocity of  $^{12}\text{CO}$  6–5 with lower outflow force.
- Kinetic temperatures of  $\sim 100$  K are found for the molecular gas in most flows studied here. Such temperatures agree with expected conditions of jet driven flows modelled by (Hatchell et al. 1999). Only the flows of L 1551 IRS 5 and IRAS 12496-7650 are much colder ( $< 50$  K), in agreement with the “fossil”, empty nature of the flows.
- The very strong intensities at all positions of RCRA IRS 7, an order of magnitude higher than can be produced by passive heating, must be due to a significant PDR region near the source. Likely, RCRA itself heats the outside of the RCRA IRS 7 envelope and cloud region.

Spatially resolved observations with APEX-CHAMP<sup>+</sup> of high- $J$  CO and isotopologues clearly provide unique insight into the structure and physical processes of low-mass protostars, as well as their feedback on the surroundings. The ubiquitous photon

**Table 7.** Outflow kinetic temperature estimates<sup>a</sup>.

Source	Ratio <sup>b</sup> K	$T_{\text{kin}}(\text{Blue})$ K	Ratio <sup>b</sup>	$T_{\text{kin}}(\text{Red})$
RCRA IRS 7	1	>200	2.5	160
NGC 1333 IRS 2	—	—	—	—
L 1551 IRS 5 <sup>c</sup>	>8	<50	9	40
TMR 1 <sup>d</sup>	1.5	180	>4	120
IRAS 12496-7650	>8	<65	—	—
HH 46 <sup>e</sup>	6	100	3	140
BHR 71	—	—	—	—
Ced 110 IRS 4	3	140	>7	<80

<sup>a</sup> Estimated with an ambient density of  $10^4 \text{ cm}^{-3}$ . <sup>b</sup> CO 3–2/6–5 line wing ratio. Ratios are averaged over velocity and distance from the source. See van Kempen et al. (2009) for more discussion. <sup>c</sup> CO 4–3/6–5 ratio. <sup>d</sup> Optical depth of 8 inferred for  $^{12}\text{CO}$  3–2 wings (Hogerheijde et al. 1998). <sup>e</sup> See van Kempen et al. (2009).

heating of the gas found here may have some consequences for the amount of envelope gas that can eventually collapse. Detailed multi-dimensional radiative transfer modelling, including outflow cavities are needed to directly address this question. Such models are now being developed for high-mass YSOs (Bruderer et al. 2009), and will be extended to low-mass YSOs. The UV radiation will also significantly affect the chemistry along the outflow walls, dissociating molecules like H<sub>2</sub>O to OH and O and HCN to CN. In the future, the Herschel Space Observatory will be able to map even higher  $J$  CO lines as well as H<sub>2</sub>O, OH and [O I] lines in the far-IR between 60 and 600  $\mu\text{m}$  with the PACS and HIFI instruments. Together, radiative transfer modelling, these data sets and future interferometric observations with ALMA will be able to fully characterize the physical and chemical structure of the earliest, deeply embedded stages of star formation.

**Acknowledgements.** T.v.K. and astrochemistry at Leiden Observatory are supported by a Spinoza prize and by NWO grant 614.041.004. The staff at APEX and many members of the Bonn submillimeter group are thanked for the excellent support during observations. CHAMP<sup>+</sup> is constructed with funds from NWO grant 600.063.310.10. We thank Ronald Stark for continued support of the CHAMP<sup>+</sup> project.

## References

- Adams, F. C., Lada, C. J., & Shu, F. H. 1987, ApJ, 312, 788  
 Arce, H. G., & Sargent, A. I. 2005, ApJ, 624, 232  
 Arce, H. G., Shepherd, D., Gueth, F., et al. 2007, in Protostars and Planets V, ed. B. Reipurth, D. Jewitt, & K. Keil, 245  
 Bachiller, R. 1996, ARA&A, 34, 111  
 Bachiller, R., & Tafalla, M. 1999, in The Origin of Stars and Planetary Systems, ed. C. J. Lada, & N. D. Kylafis (Dordrecht: Kluwer), 227  
 Bachiller, R., Tafalla, M., & Cernicharo, J. 1994, ApJ, 425, L93  
 Bisschop, S. E., Jørgensen, J. K., van Dishoeck, E. F., & de Wachter, E. B. M. 2007, A&A, 465, 913  
 Blake, G. A., Sandell, G., van Dishoeck, E. F., et al. 1995, ApJ, 441, 689  
 Boogert, A. C. A., Hogerheijde, M. R., Ceccarelli, C., et al. 2002, ApJ, 570, 708  
 Bottinelli, S., Ceccarelli, C., Lefloch, B., et al. 2004, ApJ, 615, 354  
 Bottinelli, S., Ceccarelli, C., Williams, J. P., & Lefloch, B. 2007, A&A, 463, 601  
 Bourke, T. L., Garay, G., Lehtinen, K. K., et al. 1997, ApJ, 476, 781  
 Bourke, T. L. 2001, ApJ, 554, L91  
 Brinch, C., Crapsi, A., Jørgensen, J. K., Hogerheijde, M. R., & Hill, T. 2007, A&A, 475, 915  
 Bruderer, S., Benz, A. O., Doty, S. D., van Dishoeck, E. F., & Bourke, T. L. 2009, ApJ, 700, 872  
 Butner, H. M., Evans, II, N. J., Lester, D. F., Levreault, R. M., & Strom, S. E. 1991, ApJ, 376, 636  
 Cabrit, S., & Bertout, C. 1992, A&A, 261, 274  
 Ceccarelli, C., Caux, E., White, G. J., et al. 1998, A&A, 331, 372  
 Ceccarelli, C., Castets, A., Caux, E., et al. 2000, A&A, 355, 1129

- Ceccarelli, C., Boogert, A. C. A., Tielens, A. G. G. M., et al. 2002, *A&A*, 395, 863
- Chandler, C. J., & Richer, J. S. 2000, *ApJ*, 530, 851
- Crapsi, A., van Dishoeck, E. F., Hogerheijde, M. R., Pontoppidan, K. M., & Dullemond, C. P. 2008, ArXiv e-prints, 801
- Di Francesco, J., Johnstone, D., Kirk, H., MacKenzie, T., & Ledwosinska, E. 2008, *ApJS*, 175, 277
- Draine, B. T., & Roberge, W. G. 1984, *ApJ*, 282, 491
- Dunham, M. M., Crapsi, A., Evans, II, N. J., et al. 2008, ArXiv e-prints, 806
- Enoch, M. L., Young, K. E., Glenn, J., et al. 2006, *ApJ*, 638, 293
- Evans, N. J., Harvey, P. M., Dunham, M. M., et al. 2007, c2d delivery document
- Flower, D. R., Le Bourlot, J., Pineau Des Forets, G., & Roueff, E. 1994, *A&A*, 282, 225
- Fridlund, C. V. M., Sandqvist, A., Nordh, H. L., & Olofsson, G. 1989, *A&A*, 213, 310
- Froebrich, D. 2005, *ApJS*, 156, 169
- Furlan, E., McClure, M., Calvet, N., et al. 2008, *ApJS*, 176, 184
- Giannini, T., Lorenzetti, D., Tommasi, E., et al. 1999, *A&A*, 346, 617
- Giannini, T., Nisini, B., & Lorenzetti, D. 2001, *ApJ*, 555, 40
- Groppi, C. E., Hunter, T. R., Blundell, R., & Sandell, G. 2007, *ApJ*, 670, 489
- Güsten, R., Baryshev, A., Bell, A., et al. 2008, SPIE Conf. Ser., 7020,
- Gutermuth, R. A., Myers, P. C., Megeath, S. T., et al. 2008, *ApJ*, 674, 336
- Hatchell, J., Fuller, G. A., & Ladd, E. F. 1999, *A&A*, 344, 687
- Hatchell, J., Fuller, G. A., Richer, J. S., Harries, T. J., & Ladd, E. F. 2007, *A&A*, 468, 1009
- Heathcote, S., Morse, J. A., Hartigan, P., et al. 1996, *AJ*, 112, 1141
- Henning, T., & Launhardt, R. 1998, *A&A*, 338, 223
- Henning, T., Pfau, W., Zinnecker, H., & Prusti, T. 1993, *A&A*, 276, 129
- Hiramatsu, M., Hayakawa, T., Tatematsu, K., et al. 2007, *ApJ*, 664, 964
- Hirano, N., Liu, S.-Y., Shang, H., et al. 2006, *ApJ*, 636, L141
- Hogerheijde, M. R., van Dishoeck, E. F., Blake, G. A., & van Langevelde, H. J. 1998, *ApJ*, 502, 315
- Hogerheijde, M. R., van Dishoeck, E. F., Salverda, J. M., & Blake, G. A. 1999, *ApJ*, 513, 350
- Hogerheijde, M. R., & van der Tak, F. F. S. 2000, *A&A*, 362, 697
- Ivezić, Z., & Elitzur, M. 1997, *MNRAS*, 287, 799
- Jørgensen, J. K. 2004, *A&A*, 424, 589
- Jørgensen, J. K., Schöier, F. L., & van Dishoeck, E. F. 2002, *A&A*, 389, 908
- Jørgensen, J. K., Schöier, F. L., & van Dishoeck, E. F. 2004, *A&A*, 416, 603
- Jørgensen, J. K., Schöier, F. L., & van Dishoeck, E. F. 2005, *A&A*, 435, 177
- Jørgensen, J. K., Johnstone, D., van Dishoeck, E. F., & Doty, S. D. 2006, *A&A*, 449, 609
- Kasemann, C., Güsten, R., Heyminck, S., et al. 2006, SPIE Conf., 6275
- Kenyon, S. J., Gomez, M., Marzke, R. O., & Hartmann, L. 1994, *AJ*, 108, 251
- Knee, L. B. G., & Sandell, G. 2000, *A&A*, 361, 671
- Lee, C.-F., & Ho, P. T. P. 2005, *ApJ*, 624, 841
- Lee, J.-E., Di Francesco, J., Bourke, T. L., Evans, II, N. J., & Wu, J. 2007, *ApJ*, 671, 1748
- Lehtinen, K., Haikala, L. K., Mattila, K., & Lemke, D. 2001, *A&A*, 367, 311
- Lehtinen, K., Harju, J., Kontinen, S., & Higdon, J. L. 2003, *A&A*, 401, 1017
- Liu, M. C., Graham, J. R., Ghez, A. M., et al. 1996, *ApJ*, 461, 334
- Lorenzetti, D., Tommasi, E., Giannini, T., et al. 1999, *A&A*, 346, 604
- Luhman, K. L., Allen, L. E., Allen, P. R., et al. 2008, *ApJ*, 675, 1375
- Maret, S., Ceccarelli, C., Caux, E., et al. 2004, *A&A*, 416, 577
- Moriarty-Schieven, G. H., & Snell, R. L. 1988, *ApJ*, 332, 364
- Motte, F., & André, P. 2001, *A&A*, 365, 440
- Neufeld, D. A., & Dalgarno, A. 1989, *ApJ*, 340, 869
- Nisini, B., Benedettini, M., Giannini, T., et al. 1999, *A&A*, 350, 529
- Nisini, B., Giannini, T., & Lorenzetti, D. 2002, *ApJ*, 574, 246
- Nutter, D. J., Ward-Thompson, D., & André, P. 2005, *MNRAS*, 357, 975
- Offner, S. S. R., Klein, R. I., McKee, C. F., & Krumholz, M. R. 2009, ArXiv e-prints
- Osorio, M., D'Alessio, P., Muzerolle, J., Calvet, N., & Hartmann, L. 2003, *ApJ*, 586, 1148
- Ossenkopf, V., & Henning, T. 1994, *A&A*, 291, 943
- Parise, B., Belloche, A., Lurini, S., et al. 2006, *A&A*, 454, L79
- Raga, A. C., de Colle, F., Kajdič, P., Esquivel, A., & Cantó, J. 2007, *A&A*, 465, 879
- Reipurth, B., & Raga, A. C. 1999, in NATO ASIC Proc. 540: The Origin of Stars and Planetary Systems, ed. C. J. Lada, & N. D. Kylafis, 267
- Reipurth, B., Chini, R., Krugel, E., Kreysa, E., & Sievers, A. 1993, *A&A*, 273, 221
- Reipurth, B., Rodríguez, L. F., Anglada, G., & Bally, J. 2002, *AJ*, 124, 1045
- Robitaille, T. P., Whitney, B. A., Indebetouw, R., Wood, K., & Denzmore, P. 2006, *ApJS*, 167, 256
- Sandell, G., & Knee, L. B. G. 2001, *ApJ*, 546, L49
- Schöier, F. L., Jørgensen, J. K., van Dishoeck, E. F., & Blake, G. A. 2002, *A&A*, 390, 1001
- Schöier, F. L., van der Tak, F. F. S., van Dishoeck, E. F., & Black, J. H. 2005, *A&A*, 432, 369
- Schöier, F. L., Jørgensen, J. K., Pontoppidan, K. M., & Lundgren, A. A. 2006, *A&A*, 454, L67
- Schuster, K. F., Harris, A. I., Anderson, N., & Russell, A. P. G. 1993, *ApJ*, 412, L67
- Schuster, K.-F., Russell, A. P. G., & Harris, A. I. 1995, *Ap&SS*, 224, 117
- Shirley, Y. L., Evans, II, N. J., & Rawlings, J. M. C. 2002, *ApJ*, 575, 337
- Spaans, M., Hogerheijde, M. R., Mundy, L. G., & van Dishoeck, E. F. 1995, *ApJ*, 455, L167
- Stark, R., Sandell, G., Beck, S. C., et al. 2004, *ApJ*, 608, 341
- Stäuber, P., Doty, S. D., van Dishoeck, E. F., Jørgensen, J. K., & Benz, A. O. 2004, *A&A*, 425, 577
- Terebey, S., Chandler, C. J., & Andre, P. 1993, *ApJ*, 414, 759
- van der Tak, F. F. S., Black, J. H., Schöier, F. L., Jansen, D. J., & van Dishoeck, E. F. 2007, *A&A*, 468, 627
- van Dishoeck, E. F., & Black, J. H. 1988, *ApJ*, 334, 771
- van Dishoeck, E. F., Blake, G. A., Jansen, D. J., & Groesbeck, T. D. 1995, *ApJ*, 447, 760
- van Kempen, T. A., Hogerheijde, M. R., van Dishoeck, E. F., et al. 2006, *A&A*, 454, L75
- van Kempen, T. A., van Dishoeck, E. F., Salter, D. M., et al. 2009, *A&A*, 498, 167
- White, G. J., Liseau, R., Men'shchikov, A. B., et al. 2000, *A&A*, 364, 741
- Whitney, B. A., Wood, K., Bjorkman, J. E., & Cohen, M. 2003a, *ApJ*, 598, 1079
- Whitney, B. A., Wood, K., Bjorkman, J. E., & Wolff, M. J. 2003b, *ApJ*, 591, 1049